

SN 2020kyg and the rates of faint Iax supernovae from ATLAS

Shubham Srivastav^{1b},¹★ S. J. Smartt,¹★ M. E. Huber,² K. C. Chambers,² C. R. Angus^{1b},³ T.-W. Chen,⁴ F. P. Callan,¹ J. H. Gillanders^{1b},¹ O. R. McBrien,⁵ S. A. Sim,¹ M. Fulton,¹ J. Hjorth,³ K. W. Smith,¹ D. R. Young,¹ K. Auchettl,^{6,7,8} J. P. Anderson,⁹ G. Pignata,^{10,11} T. J. L. de Boer,² C.-C. Lin^{1b}² and E. A. Magnier²

¹*Astrophysics Research Centre, School of Mathematics and Physics, Queen's University Belfast, Belfast BT7 1NN, UK*

²*Institute of Astronomy, University of Hawaii, 2680 Woodlawn Drive, Honolulu, HI 96822, USA*

³*DARK, Niels Bohr Institute, University of Copenhagen, Lyngbyvej 2, DK-2100 Copenhagen Ø, Denmark*

⁴*The Oskar Klein Centre, Department of Astronomy, Stockholm University, AlbaNova, SE-10691 Stockholm, Sweden*

⁵*Department of Physics, University of Warwick, Coventry CV4 7AL, UK*

⁶*School of Physics, The University of Melbourne, Melbourne VIC 3010, Australia*

⁷*ARC Centre of Excellence for All Sky Astrophysics in 3 Dimensions (ASTRO 3D), Australia*

⁸*Department of Astronomy and Astrophysics, University of California, Santa Cruz, CA 95064, USA*

⁹*European Southern Observatory, Alonso de Córdova 3107, Casilla 19, Santiago, Chile*

¹⁰*Departamento de Ciencias Físicas, Universidad Andrés Bello, Fernández Concha 700, Las Condes, Santiago, Chile*

¹¹*Millennium Institute of Astrophysics (MAS), Nuncio Monsenor Sòtero Sanz 100, Providencia, Santiago, Chile*

Accepted 2022 January 14. Received 2022 January 7; in original form 2021 November 18

ABSTRACT

We present multiwavelength follow-up observations of the ATLAS discovered faint Iax supernova SN 2020kyg that peaked at an absolute magnitude of $M_g \approx -14.9 \pm 0.2$, making it another member of the faint Iax supernova population. The bolometric light curve requires only $\approx 7 \times 10^{-3} M_\odot$ of radioactive ^{56}Ni , with an ejected mass of $M_{\text{ej}} \sim 0.4 M_\odot$ and a low kinetic energy of $E \approx 0.05 \pm 0.02 \times 10^{51}$ erg. We construct a homogeneous volume-limited sample of 902 transients observed by ATLAS within 100 Mpc during a 3.5 yr span. Using this sample, we constrain the rates of faint Iax ($M_r \gtrsim -16$) events within 60 Mpc at 12_{-8}^{+14} per cent of the SN Ia rate. The overall Iax rate, at 15_{-9}^{+17} per cent of the Ia rate, is dominated by the low-luminosity events, with luminous SNe Iax ($M_r \lesssim -17.5$) like 2002cx and 2005hk, accounting for only $0.9_{-0.5}^{+1.1}$ per cent of the Ia rate (a 2σ upper limit of approximately 3 per cent). We favour the hybrid CONe WD + He star progenitor channel involving a failed deflagration of a near Chandrasekhar mass white dwarf, expected to leave a bound remnant and a surviving secondary companion, as a candidate explanation for faint Iax explosions. This scenario requires short delay times, consistent with the observed environments of SNe Iax. Furthermore, binary population synthesis calculations have suggested rates of 1–18 per cent of the SN Ia rate for this channel, consistent with our rate estimates.

Key words: supernovae: general – supernovae: individual: SN 2020kyg.

1 INTRODUCTION

Supernovae of Type Ia (SNe Ia) are widely considered to be thermonuclear explosions involving at least one white dwarf (WD) star in a close binary system (Maoz, Mannucci & Nelemans 2014; Livio & Mazzali 2018). SNe Ia are known for being remarkably homogeneous with standardizable light curves that enable them to be used as cosmic distance indicators (Phillips 1993; Hamuy et al. 1996), leading to the discovery of the accelerating expansion of the Universe (Riess et al. 1998; Perlmutter et al. 1999). However, open questions regarding the nature of the progenitors and explosion mechanisms remain. Their use as cosmic probes notwithstanding, a rich diversity in the observed properties of SNe Ia is undeniably present (Taubenberger 2017).

SNe Iax comprise a peculiar subclass of SNe Ia (Li et al. 2003; Foley et al. 2013), characterized by lower ejecta velocities of $\sim 2000\text{--}7000 \text{ km s}^{-1}$ (Jha 2017), as opposed to typical expansion velocity of $\gtrsim 10\,000 \text{ km s}^{-1}$ observed in normal SNe Ia around maximum light (Folatelli et al. 2013). Despite the lower velocities, the early spectra of SNe Iax are known to show similarities with SNe Ia, in particular SN 1991T-like and SN 1999aa-like SNe Ia (Foley et al. 2013; McCully et al. 2014b). Later spectra of SNe Iax, however, unlike normal SNe Ia, tend to show persistent low-velocity permitted lines of Fe II and Ca II, in addition to forbidden lines of [Fe II], [Ni II], and [Ca II] (e.g. Jha et al. 2006; Sahu et al. 2008). SNe Iax constitute a very heterogeneous subclass with rich diversity in line velocities, relative strengths, and line widths of permitted and forbidden transitions, especially in later spectra (McCully et al. 2014b; Stritzinger et al. 2015; Yamanaka et al. 2015; Foley et al. 2016). Magee et al. (2017) noted that spectra of the Iax event

* E-mail: shubhamsrivastav@gmail.com (SS); S.Smartt@qub.ac.uk (SJS)

PS1-12bwh around maximum closely resembled spectra of SN 2005hk at phases approximately a week earlier, implying lower densities for the high velocity ejecta in PS1-12bwh relative to SN 2005hk. This diversity is also reflected in photometric properties, with SNe Iax exhibiting a wide range of decline rates, rise times, and peak luminosities (Magee et al. 2016).

The nearby Iax SN 2012Z is the only SN Ia with an identified progenitor system in deep pre-explosion *HST* images, where the blue source was identified as a helium-rich companion to the WD (McCully et al. 2014a). Follow-up *HST* imaging ~ 1400 d after explosion shows that the source has not disappeared (McCully et al. 2022). A potential companion was also detected in the case of SN 2008ha by Foley et al. (2014) in *HST* images ~ 4 yr after explosion. Pure deflagration models (Jordan et al. 2012; Kromer et al. 2013) of Chandrasekhar mass (M_{Ch}) WDs in a single degenerate system that result in either partial or complete disruption of the WD have had success in reproducing the low kinetic energies and a range of luminosities (except for the faint end of the distribution) observed in SNe Iax. These weak ‘failed’ explosions are thus thought to leave behind a bound remnant enriched with the deflagration ashes (Jordan et al. 2012; Fink et al. 2014). A similar model involving a hybrid carbon-oxygen-neon (CONE) WD instead of a CO WD was invoked by Kromer et al. (2015) to explain the faintest members of the subclass. Recent simulations by Lach et al. (2021) show that deflagrations of CO WDs can also produce faint explosions with peak absolute magnitudes of $M_r \approx -15$. The bound remnant picture is promising, since an optically thick wind from the remnant (Foley et al. 2016; Shen & Schwab 2017) would help explain the long-lived photosphere and the fact that the spectra do not become nebular even at later epochs. It can also potentially explain the late-time flattening observed in the light curves of SNe Iax (e.g. McCully et al. 2014b; Singh et al. 2018; Kawabata et al. 2018, 2021; McCully et al. 2022). However, the radiation physics involving the bound remnant is complicated and our current theoretical insights regarding the long-term evolution of these bound remnants, or postgenitors, are limited (Zhang et al. 2019).

Of particular interest are the least luminous and least energetic members of the subclass – events like SNe 2021fcg (Karambelkar et al. 2021), 2008ha (Foley et al. 2009; Valenti et al. 2009; Stritzinger et al. 2014), 2010ae (Stritzinger et al. 2014), and 2019gsc (Srivastav et al. 2020; Tomasella et al. 2020). With $M_g \lesssim -14$, SN 2019gsc synthesized a meagre $2 \times 10^{-3} M_{\odot}$ of radioactive ^{56}Ni . These ‘faint Iax’ events show peak luminosity and kinetic energy that is lower than that of normal SNe Ia by a factor of a few hundred, posing a challenge for theoretical models to reproduce these extreme properties. Although a core-collapse origin for SN 2008ha was proposed by Valenti et al. (2009), the photometric and spectroscopic properties of these faint objects seem to align more closely with the overall population of SNe Iax (Jha 2017). In particular, the unambiguous detection of Co II lines in the near-infrared (NIR) spectra of lower luminosity Iax events SN 2010ae (Stritzinger et al. 2014) and SN 2019muj (Barna et al. 2021), also seen in more luminous members like SN 2014ck (Tomasella et al. 2016), suggests a kinship with more luminous SNe Iax and the general Ia population. Although the deflagration model of a hybrid CONe WD (Kromer et al. 2015) yields extremely faint transients with peak *B*-band luminosity between -13.2 and -14.6 , consistent with faint SNe Iax, it also produces very low ejecta masses ($\sim 0.01 M_{\odot}$), an order of magnitude lower than that inferred from observations, leading to much faster predicted decline rate.

The volumetric rates of SNe Iax are not particularly well-constrained, ranging from roughly 5–30 per cent of the total SN Ia

rate (Li et al. 2011; Foley et al. 2013). Also, SNe Iax seem to occur preferentially in young stellar populations (e.g. Lyman et al. 2018; Hakobyan et al. 2020), suggesting the progenitors have short delay times (Takaro et al. 2020), in turn suggesting more massive WD progenitors, which would attain M_{Ch} in a shorter time (Jha 2017). An intriguing alternative to the single degenerate scenario for SNe Iax is a double degenerate merger scenario, involving a primary ONe WD and a secondary CO WD (Kashyap et al. 2018); or a WD and a neutron star or black hole (NS/BH, Fernández & Metzger 2013). The ONe–CO WD merger model of Kashyap et al. (2018) yields an extremely faint transient with $M_V = -11.3$, roughly three times less luminous than SN 2021fcg, the faintest Iax event discovered to date (Karambelkar et al. 2021). A ONe WD – NS/BH merger explored by Bobrick et al. (2022) can theoretically produce relatively faint (up to $M \sim -16.5$), but rather long-lived and red transients. There is one observed example of such a proposed merger, AT 2018kzr (McBrien et al. 2019; Gillanders, Sim & Smartt 2020). However, this transient was fast declining and relatively blue (McBrien et al. 2019), and the composition from spectral modelling suggested a significant amount of ^{54}Fe was present (Gillanders et al. 2020). Hence, there is no clear consensus on what a WD + NS/BH merger should look like in the optical and NIR.

In this paper, we present results of multiwavelength observations of the faint Iax SN 2020kyg. We also constrain the volumetric rates of Iax and faint Iax events using a 3.5 yr sample of transients within 100 Mpc observed by the Asteroid Terrestrial-impact Last Alert System (ATLAS) survey.

2 DISCOVERY AND FOLLOW-UP OBSERVATIONS

We discovered SN 2020kyg (as ATLAS20nuc, Fig. 1) with the ATLAS (Tonry et al. 2018) in images taken on 2020 May 24.4 UT or MJD 58993.4, at an orange-band magnitude of $o = 18.83$ (Smith et al. 2020a). The data from ATLAS are processed in real time, initially on site and then the detections are filtered on our ATLAS Transient Server at Queen’s University Belfast (Smith et al. 2020b). SN 2020kyg was discovered within the same night (as is now routine), with a human scanner recognizing it 3.6 h after the quad of nightly ATLAS images at that position was completed. We registered the discovery on the IAU Transient Name Server (TNS) as AT 2020kyg on 2020 May 24.55 UT, noting that it was a young object likely associated with host galaxy NGC 5012, with a non-detection in ATLAS 4 d before (Smith et al. 2020a). It was rapidly classified as a SN Iax independently by Ochner et al. (2020) and Hiramatsu et al. (2020), with spectra taken 0.40 and 0.88 d after the discovery announcement on the TNS, respectively. ATLAS continued to observe the field until MJD 59077 (2020 August 16), or 84 d after discovery, providing good photometric sampling. We supplemented this with multicolour optical to NIR photometry from different observing facilities discussed below. The ATLAS data are publicly available from our forced photometry server¹ (Shingles et al. 2021).

2.1 Photometry

Following the classification, we triggered initial follow-up photometry from the Robotic 2m Liverpool Telescope (Steele et al. 2004). Images were obtained in the Sloan *ugriz* bands using the 4k x 4k IO:O instrument. Basic data reductions, including bias subtraction,

¹<https://fallingstar.com/forcedphot>

overscan trimming, and flat-field corrections were performed automatically by the IO:O pipeline, and the processed images were downloaded from the LT data archive. Point-spread function (PSF) photometry was performed on the images and the SN magnitudes were estimated by calibrating the zero-points against PS1 reference stars in the field of view. No image subtraction was applied since the SN was relatively bright at this epoch and is significantly offset (~ 35 arcsec) from its host.

As the transient evolved and faded, optical photometric follow-up was obtained using the 1.8m Pan-STARRS1 (PS1) telescope (Chambers et al. 2016). PS1 uses the 1.4 Gigapixel camera GPC1 with a pixel scale of 0.26 arcsec. Photometry was obtained in the *grizy_{P1}* filter system described in Tonry et al. (2012). The images were processed with the Image Processing Pipeline (IPP; Magnier et al. 2020a) and image subtraction was performed using the PS1 Science Consortium (PS1SC; Chambers et al. 2016) 3π survey data as reference. Instrumental magnitudes were computed using PSF photometry and calibrations were performed using zero-points calculated using PS1 reference stars in the field (Magnier et al. 2020b; Waters et al. 2020). We also triggered NIR photometry in *JHK* bands on the Wide Field Infrared Camera (WFCAM) on the United Kingdom Infrared Telescope (UKIRT) at Maunakea, Hawaii. WFCAM has four 2048×2048 HgCdTe detectors, with a pixel scale of 0.4 arcsec and a 0.2 square degree field of view. The processed data were obtained from the Cambridge Astronomy Survey Unit. The dithered frames in each filter were resampled and co-added using the SWARP package (Bertin et al. 2002). PSF photometry was performed on the co-added frames and the zero-points were calibrated using the 2MASS catalog (Skrutskie et al. 2006). No image subtraction was done for the NIR images.

SN 2020kyg was followed up by the UVOT instrument (Romig et al. 2005) aboard the *Swift* observatory (Gehrels et al. 2004). The images were obtained in broadband filters *v* (5468 Å), *b* (4392 Å), *u* (3465 Å), *uvw1* (2600 Å), *uvw2* (2246 Å), and *uvw2* (1928 Å). The processed images were downloaded from the *Swift* archive. The individual frames for each observation ID in a given filter were co-added using the `uvot_ismsum` task within the High Energy Astrophysics SOFTWARE (HEASOFT) package. Photometry was performed on the co-added frames with the `uvot_source` task using a 5 arcsec aperture, following the recipe of Poole et al. (2008) and Brown et al. (2009), using updated zero-points and effective area curves for the UVOT filters (Breeveld et al. 2011). Since archival images of the field were available in *u*, *uvw1*, *uvw2*, and *uvw2*, the magnitudes in these filters were estimated after subtraction of the underlying galaxy flux. To perform the template subtraction, we adopt the method outlined by Brown et al. (2014). The count rates in the template frames (for a 5 arcsec aperture) were subtracted from the count rates in the SN frames, before applying an aperture correction. The detections in the *uvw1*, *uvw2*, and *uvw2* images are marginal ($< 5\sigma$), and we only use the *u* magnitudes in the subsequent analysis. Once the supernova had faded significantly in the *u*-band ($u_{AB} > 21$), we triggered deep *u*-band imaging observations on the 3.6m Canada-France-Hawaii Telescope (CFHT) at Maunakea. The images were obtained with the wide-field MegaCam instrument consisting of 40 2048×4612 pixel CCDs with a 0.2 arcsec pixel scale and a 1 square degree field of view. The processed and astrometrically calibrated images were obtained from the Data Archiving and Distribution System. For each epoch, the individual exposures were aligned and co-added using SWARP and PSF photometry was performed to estimate instrumental magnitudes. The SN instrumental magnitudes were calibrated using zero-points calculated from local reference stars in the SDSS catalog. The CFHT images are much deeper than the SDSS *u*-band reference frames of

the field, thus no image subtraction was performed. The photometric magnitudes are summarized in Table 1.

2.2 Spectroscopy

The initial two epochs of spectroscopic observations on 2020 May 30 and May 31 were obtained with the SPectrograph for the Rapid Acquisition of Transients (SPRAT; Piascik et al. 2014) on the LT while the SN was relatively bright. The wavelength and flux calibrated 1D spectra were obtained from the SPRAT pipeline. The default extraction parameters on the pipeline generally work well for isolated point sources. Since SN 2020kyg is significantly offset from its host galaxy, the quality of the extraction was adequate and a manual extraction in IRAF² does not discernibly enhance the signal-to-noise.

Subsequent spectroscopic observations during two epochs were obtained with the Alhambra Faint Object Spectrograph and Camera (ALFOSC) on the Nordic Optical Telescope (NOT) at La Palma on 2020 June 13 and June 21 using grism 4 and a 1.0 arcsec slit, aligned along the parallactic angle. Both observations were conducted under clear observing conditions and good seeing. The spectra were reduced using a custom pipeline running standard PYRAF procedures.

We obtained two final epochs of spectroscopic observations on 2020 July 10 and July 21, with the Gemini Multi-Object Spectrograph (GMOS-N) instrument on Gemini North. The Gemini spectra were obtained using the R400 grating ($R \approx 1900$) and a 1 arcsec slit, and reduced with various tasks in the Gemini IRAF package.

Finally, in order to tie the spectra to an absolute flux scale, we computed synthetic photometry for the spectra using the Synthetic Magnitudes from Spectra code (SMS; Inserra et al. 2018). The broadband *ugrizy* photometry described above was used to compute monochromatic fluxes that were interpolated at epochs corresponding to the spectroscopic observations, and a scaling factor was applied to the spectra where necessary.

3 LIGHT CURVES AND EXPLOSION PARAMETERS

The median redshift independent distance on the NASA Extragalactic Database (NED) for the host galaxy NGC 5012 from 18 different measurements, scaled to $H_0 = 70 \text{ km s}^{-1} \text{ Mpc}^{-1}$, is 41 Mpc. The three most recent Tully-Fisher (TF) distances from Spitzer 3.8 μm (Sorice et al. 2014) and *I*-band data (Tully, Courtois & Sorice 2016) are between 42 and 43 Mpc (for an adopted $H_0 = 75 \text{ km s}^{-1}$), consistent with the median value stated above. The Hubble Flow distance, from the dynamically corrected recessional velocity (3169 km s^{-1}) is also similar at $45 \pm 3 \text{ Mpc}$. We adopt the mean of the three recent TF measurements scaled to $H_0 = 70 \text{ km s}^{-1} \text{ Mpc}^{-1}$, i.e. $d = 43 \pm 3 \text{ Mpc}$ or a distance modulus $\mu = 33.17 \pm 0.15$ for SN 2020kyg. A standard reddening law with $R_V = 3.1$ and $A_V = 0.038 \text{ mag}$ (Schlafly & Finkbeiner 2011) was adopted to correct for Galactic extinction along the line of sight. The reddening due to the host galaxy was assumed to be negligible, since SN 2020kyg is significantly offset from the host, and there is no sign of narrow Na I lines in the spectra. Thus, a

²IRAF is distributed by the National Optical Astronomy Observatory, which is operated by the Association of Universities for Research in Astronomy (AURA) under a cooperative agreement with the National Science Foundation.

Table 1. Summary of photometric observations in *ugrizy/JHK* bands for SN 2020kyg. All magnitudes are in the AB system.

MJD	<i>u</i>	<i>g</i>	<i>r</i>	<i>i</i>	<i>z</i>	<i>y</i>	<i>J</i>	<i>H</i>	<i>K</i>	Instrument
58991.26	-	20.03 ± 0.35	20.03 ± 0.14	-	-	-	-	-	-	ZTF
58994.94	-	18.43 ± 0.01	18.49 ± 0.02	18.66 ± 0.03	18.82 ± 0.028	-	-	-	-	LT
58995.22	18.86 ± 0.12	-	-	-	-	-	-	-	-	UVOT
58996.03	18.96 ± 0.12	-	-	-	-	-	-	-	-	UVOT
58998.75	19.36 ± 0.17	-	-	-	-	-	-	-	-	UVOT
58999.28	19.59 ± 0.16	-	-	-	-	-	-	-	-	UVOT
58999.89	-	18.39 ± 0.02	18.29 ± 0.02	18.40 ± 0.03	18.46 ± 0.03	-	-	-	-	LT
59000.89	-	18.50 ± 0.02	18.32 ± 0.02	18.40 ± 0.03	18.43 ± 0.03	-	-	-	-	LT
59003.39	20.30 ± 0.20	-	-	-	-	-	-	-	-	UVOT
59005.18	21.31 ± 0.27	-	-	-	-	-	-	-	-	UVOT
59006.34	-	19.05 ± 0.07	18.36 ± 0.03	18.42 ± 0.03	18.35 ± 0.02	18.48 ± 0.05	-	-	-	PSI
59009.11	21.65 ± 0.28	-	-	-	-	-	19.36 ± 0.08	19.40 ± 0.18	19.86 ± 0.33	UVOT
59010.24	-	-	-	-	-	-	-	-	-	UKIRT
59010.36	-	19.65 ± 0.09	18.63 ± 0.03	18.61 ± 0.03	18.56 ± 0.06	18.57 ± 0.11	-	-	-	PSI
59013.34	-	20.00 ± 0.08	18.77 ± 0.04	18.80 ± 0.05	18.76 ± 0.09	18.74 ± 0.23	-	-	-	PSI
59014.27	-	-	-	-	-	-	19.40 ± 0.18	19.53 ± 0.18	-	UKIRT
59016.34	-	20.24 ± 0.07	19.02 ± 0.03	18.88 ± 0.03	18.87 ± 0.05	19.02 ± 0.11	-	-	-	PSI
59017.31	-	-	-	-	-	-	19.49 ± 0.08	-	20.07 ± 0.31	UKIRT
59020.27	22.70 ± 0.18	-	-	-	-	-	-	-	-	CFHT
59021.28	-	20.40 ± 0.05	19.26 ± 0.02	19.15 ± 0.02	19.01 ± 0.03	19.12 ± 0.07	-	-	-	PSI
59021.29	22.82 ± 0.17	-	-	-	-	-	-	-	-	CFHT
59024.24	-	-	-	-	-	-	19.76 ± 0.14	19.96 ± 0.19	-	UKIRT
59025.26	23.05 ± 0.19	-	-	-	-	-	19.88 ± 0.11	19.96 ± 0.19	-	CFHT
59026.27	-	20.71 ± 0.10	19.58 ± 0.04	19.48 ± 0.05	19.27 ± 0.06	19.41 ± 0.13	-	-	-	UKIRT
59029.27	-	20.86 ± 0.09	19.66 ± 0.04	19.57 ± 0.03	19.21 ± 0.03	19.52 ± 0.09	-	-	-	CFHT
59032.30	-	-	19.85 ± 0.08	19.74 ± 0.09	19.43 ± 0.09	19.44 ± 0.18	-	-	-	UKIRT
59034.27	-	-	-	-	-	-	20.41 ± 0.15	-	-	PSI
59035.36	-	-	20.01 ± 0.30	19.74 ± 0.16	19.42 ± 0.15	-	-	-	-	PSI
59036.27	-	-	-	-	-	-	-	20.35 ± 0.23	-	UKIRT
59037.29	-	-	-	-	-	-	-	-	21.03 ± 0.35	UKIRT
59040.28	-	21.08 ± 0.16	20.12 ± 0.14	19.94 ± 0.13	19.80 ± 0.18	-	20.60 ± 0.14	-	-	PSI
59041.26	-	-	-	-	-	-	-	-	-	UKIRT
59041.28	23.69 ± 0.23	-	-	-	-	-	-	-	-	CFHT
59042.26	23.92 ± 0.30	-	-	-	-	-	-	-	-	CFHT
59043.27	23.85 ± 0.23	-	-	-	-	-	-	-	-	CFHT
59047.29	-	21.22 ± 0.10	20.21 ± 0.06	20.09 ± 0.09	19.71 ± 0.10	20.06 ± 0.26	-	-	-	PSI
59048.26	-	-	-	-	-	-	20.81 ± 0.19	-	-	UKIRT
59048.29	24.02 ± 0.22	-	-	-	-	-	-	-	-	CFHT
59051.26	24.13 ± 0.32	-	-	-	-	-	-	-	-	CFHT
59052.28	-	21.37 ± 0.26	20.39 ± 0.13	20.36 ± 0.13	19.83 ± 0.14	19.82 ± 0.30	-	-	-	PSI
59054.26	-	-	-	-	-	-	-	20.84 ± 0.23	-	UKIRT
59058.28	-	-	20.44 ± 0.26	20.48 ± 0.20	-	-	-	-	-	PSI
59064.28	-	-	20.53 ± 0.32	20.53 ± 0.26	20.30 ± 0.28	-	-	-	-	PSI
59074.26	-	-	20.78 ± 0.23	20.64 ± 0.19	20.34 ± 0.25	-	-	-	-	PSI

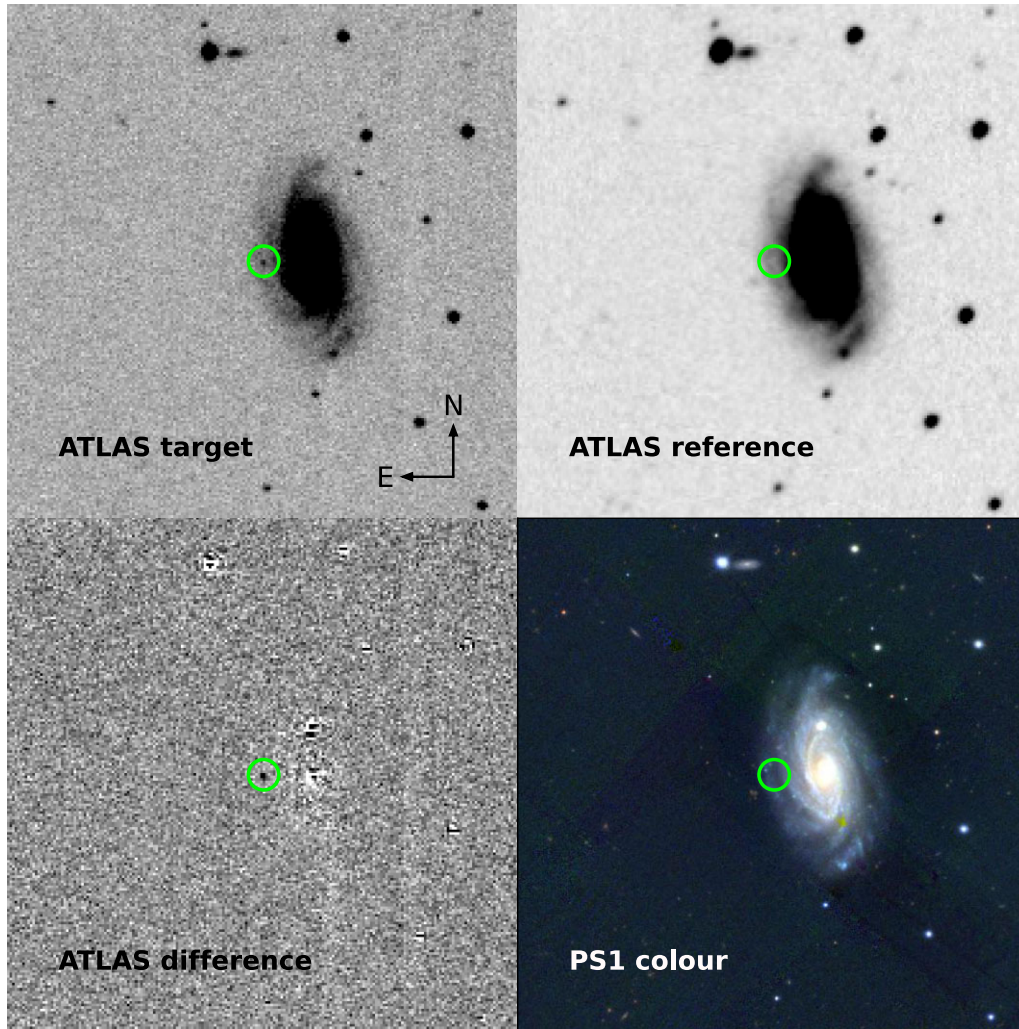


Figure 1. ATLAS target, reference, and difference images for SN 2020kyg. Also shown is the colour-composite PS1 image.

total reddening of $A_V = 0.038$ mag was adopted for SN 2020kyg in the subsequent analysis.

3.1 Light-curve properties

The multiband light curves of SN 2020kyg are shown in Fig. 2. The explosion epoch is well constrained with a combination of ATLAS and Zwicky Transient Facility (ZTF) data. There are detections by ZTF (Bellm et al. 2019) 2 d before the ATLAS discovery, although with one being marginal it was not registered as a discovery on MJD 58991.3. The ZTF photometry (through the Lasair broker; Smith et al. 2019) reports a 3σ detection at $g = 20.03 \pm 0.36$ and a more secure detection at $r = 20.03 \pm 0.14$, with ATLAS non-detections on MJDs 58985.38 ($\sigma > 20.15$) 58987.39 ($c > 20.52$) and MJD 58989.35 ($\sigma > 20.28$). SN 2020kyg was discovered a few days before peak and the pre-maximum photometric coverage is not adequate to allow a precise estimate for the explosion epoch using an expanding fireball model. The epoch of explosion was instead estimated from the best-fitting rise time from modelling the bolometric light curve (Section 3.2).

The light-curve parameters, including peak absolute magnitudes, decline rates and rise times, estimated using polynomial fits, are

summarized in Table 2. The uncertainties on the peak luminosity were estimated by combining in quadrature the error on the peak observed magnitude from the polynomial fit, and error on distance modulus, $\mu = 33.17 \pm 0.15$ mag. The r -band light curve peaks at an absolute magnitude $M_r = -14.91 \pm 0.15$, placing it among the least luminous thermonuclear SNe observed. SN 2020kyg shows a modest decline rate in the r -band, $\Delta m_{15}(r) = 0.67 \pm 0.05$, in contrast to faint Iax events such as SN 2019gsc with $\Delta m_{15}(r) = 0.91 \pm 0.09$ (Srivastav et al. 2020), SN 2010ae with $\Delta m_{15}(r) = 1.01 \pm 0.03$ and SN 2008ha with $\Delta m_{15}(r) = 1.11 \pm 0.04$ (Stritzinger et al. 2014). The r -band decline rate of SN 2020kyg is comparable to more luminous members of the Iax family such as SNe 2005hk (Stritzinger et al. 2015) and 2015H (Magee et al. 2016) and the normal SN Ia population rather than other members of the faint Iax sample. This is in keeping with the heterogeneity seen in SN Iax light curves (Magee et al. 2016).

The absolute magnitude light curves of SN 2020kyg in $grizJH$ bands are shown in Fig. 3, along with those of Iax SNe 2019gsc (Srivastav et al. 2020), 2010ae (Stritzinger et al. 2014), 2008ha (Stritzinger et al. 2014), and 2005hk (Phillips et al. 2007). The peak luminosity is known to be correlated with the decline rate in SNe Iax (e.g. Foley et al. 2013; Magee et al. 2016; Jha 2017), akin

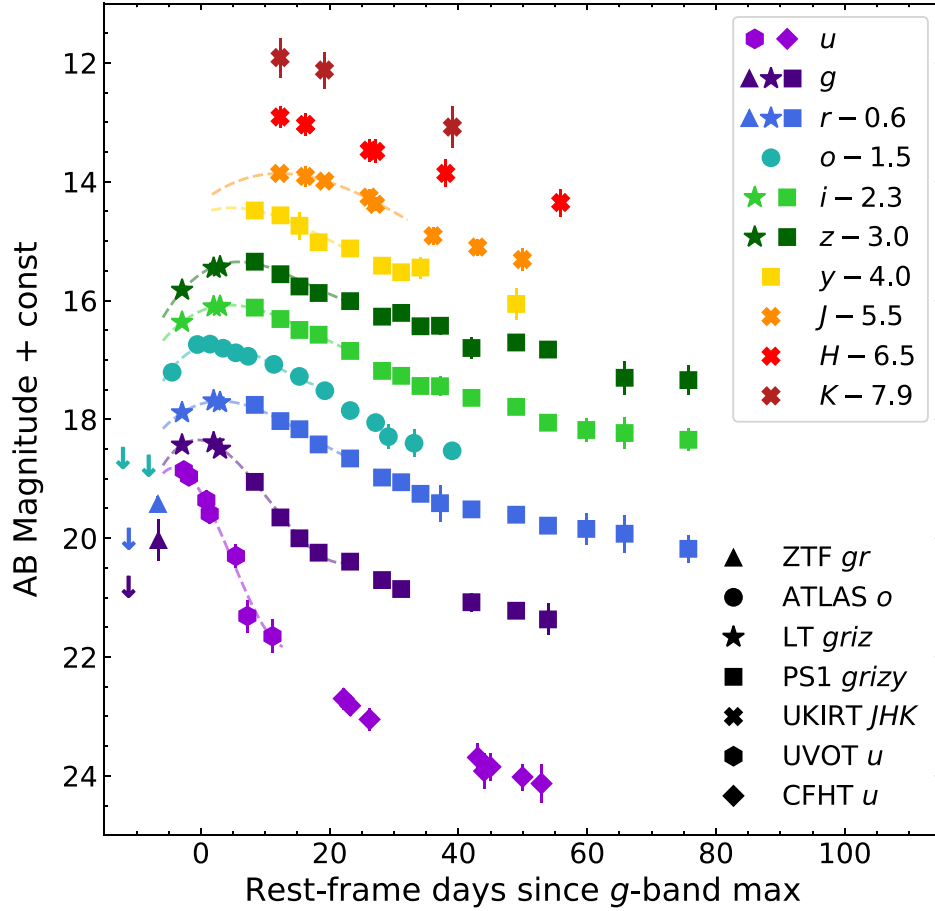


Figure 2. Multicolour *ugrizyJHK* light curves of SN2020kyg. All magnitudes are in the AB system. The light curves were shifted in the y-axis for clarity. ATLAS *o*-band, ZTF *g* and *r*-band non-detections prior to discovery are also shown. The different symbols represent different observing facilities, as shown in the legend.

Table 2. Light-curve parameters for SN 2020kyg. The peak absolute magnitudes were computed for a distance modulus $\mu = 33.17 \pm 0.15$ mag and corrected for Galactic extinction along the line of sight. The uncertainties on the peak luminosity include the uncertainty on the distance modulus and the peak magnitude derived from the polynomial fit. All magnitudes are in the AB system. The rise time in each band was estimated assuming the epoch of explosion as MJD 58988.0 ± 1.5 (Section 3.2).

Filter	T_{peak}	Peak Obs. Mag	Peak Abs. Mag	Δm_{15}	Rise Time
<i>u</i>	58993.7	18.81 ± 0.17	-14.41 ± 0.23	2.81 ± 0.29	5.7
<i>g</i>	58997.5	18.35 ± 0.03	-14.87 ± 0.15	1.53 ± 0.12	9.5
<i>r</i>	59001.0	18.29 ± 0.03	-14.91 ± 0.15	0.67 ± 0.05	13.0
<i>o</i>	59000.5	18.23 ± 0.11	-14.97 ± 0.19	0.68 ± 0.13	12.5
<i>i</i>	59002.3	18.38 ± 0.06	-14.82 ± 0.16	0.57 ± 0.07	14.3
<i>z</i>	59003.8	18.35 ± 0.06	-14.84 ± 0.16	0.58 ± 0.08	15.8
<i>y</i>	59002.7	18.44 ± 0.12	-14.74 ± 0.19	0.53 ± 0.14	14.7
<i>J</i>	59009.9	19.36 ± 0.18	-13.81 ± 0.23	0.49 ± 0.16	21.9
<i>H</i>	–	–	≤ -13.77	–	–
<i>K</i>	–	–	≤ -13.31	–	–

to the general Ia population, although the relation is much steeper in SNe Iax given the wide range in luminosity. Following Magee et al. (2016), Fig. 4 shows the peak absolute *r*-band magnitude as a function of *r*-band decline rate for several SNe Iax, along with the normal Ia population for context. The parameters for normal SNe Ia were computed from the Carnegie Supernova Project (CSP) data

(Stritzinger et al. 2011; Krisciunas et al. 2017). The *r*-band light curve for each object in the CSP sample, with adequate coverage around maximum, was fit with a polynomial function to estimate the epoch of maximum, peak observed magnitude and decline rate. The distances were derived from the redshift (scaled to $H_0 = 70 \text{ km s}^{-1} \text{ Mpc}^{-1}$) and peak absolute magnitudes were computed after correcting for

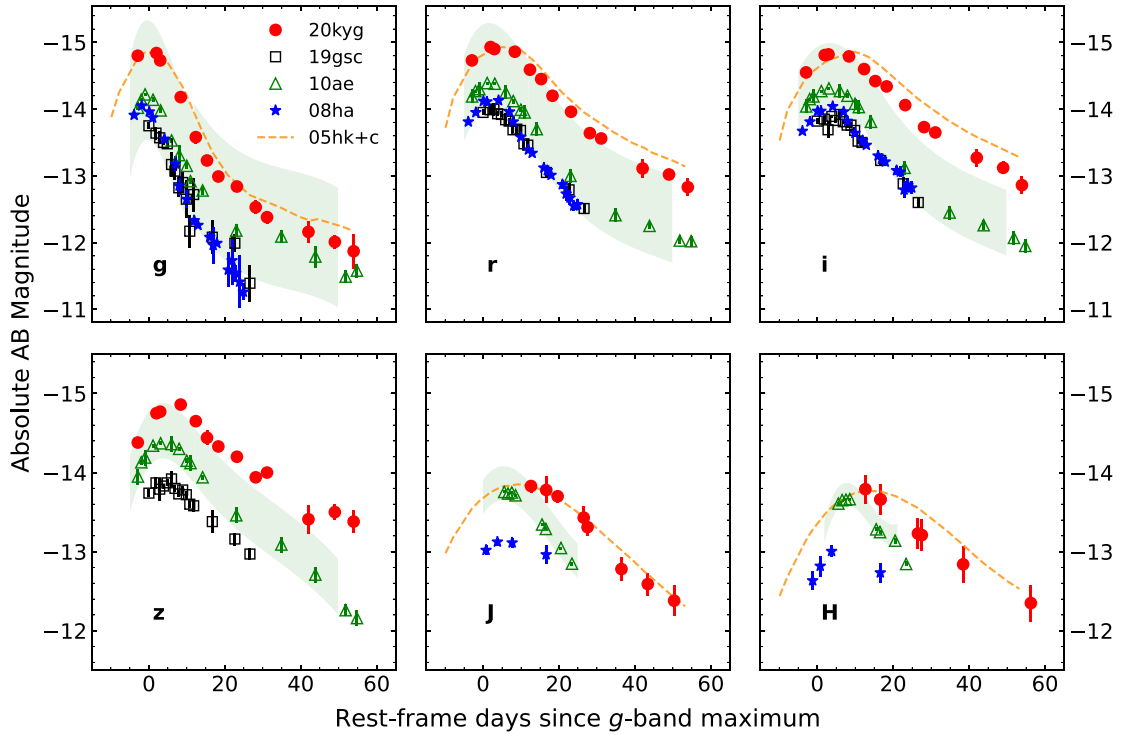


Figure 3. Absolute magnitude light curves of SN 2020kyg in *grizJH* bands, compared with the Iax events SNe 2019gsc, 2010ae, 2008ha, and 2005hk. For SN 2010ae, we adopt $E(B - V)_{\text{tot}} = 0.3$ (Srivastav et al. 2020). The shaded region indicates the range of absolute magnitudes for SN 2010ae given the large uncertainty in the reddening, $E(B - V)_{\text{tot}} = 0.62 \pm 0.42$ (Stritzinger et al. 2014). The light curves of SN 2005hk were shifted by ~ 3 magnitudes in each band to match the peak absolute magnitudes of SN 2020kyg.

Galactic extinction. Photometric outliers in the CSP Ia sample were rejected by imposing the criterion $-19.5 \leq M_r^{\text{peak}} \leq -18.5$. The objects highlighted in magenta are Iax events from our ATLAS 100 Mpc Local Volume Survey (described further in Section 5), used to estimate true volumetric rates. For the Iax events SNe 2019ovu, 2020sck, and 2020udy, the peak *r*-band absolute magnitude was estimated from the ATLAS cyan and orange-band peak magnitudes, as $M_r \approx 0.35M_c + 0.65M_o$ (Tonry et al. 2018).

3.2 Bolometric light curve

The multicolour *ugrizyJHK* photometry of SN 2020kyg was used to compute the integrated quasi-bolometric flux using the `SuperBol` code (Nicholl 2018). In addition to the quasi-bolometric flux integrated within the limits defined by the photometric passbands, `SuperBol` also computes a full blackbody integration from a fit to the spectral energy distribution (SED) to account for missing flux. However, due to heavy line blanketing in the ultraviolet (UV) regime, a full blackbody extrapolation would likely overestimate the bolometric flux. The full *ugrizyJHK* (top panel) and the *ugrizy* (middle panel) quasi-bolometric light curve of SN 2020kyg is shown in Fig. 5, along with the quasi-bolometric light curves of the faint Iax SNe 2008ha (Foley et al. 2009; Stritzinger et al. 2014), 2010ae (Stritzinger et al. 2014), 2019gsc (Srivastav et al. 2020), the intermediate luminosity Iax SN 2019muj (Barna et al. 2021), and the luminous Iax SN 2005hk (Phillips et al. 2007) for comparison. The quasi-bolometric light curves of all the objects were computed using the same method for consistency and direct comparison. The magnitudes for each SN were corrected for extinction assuming a standard reddening law with $R_V = 3.1$ prior to computing the

bolometric fluxes. The total $E(B - V)$ values adopted were 0.09 for SN 2005hk (Phillips et al. 2007), 0.08 for SN 2008ha (Foley et al. 2009), 0.30 for SN 2010ae (Srivastav et al. 2020), 0.02 for SN 2019muj (Barna et al. 2021), and 0.01 for SN 2019gsc (Srivastav et al. 2020). Also shown in Fig. 5 is the evolution of effective blackbody temperature computed from the fit of a Planck function to the observed object SEDs (photometry available in all passbands was used for the fit). The blackbody temperature evolution of all these objects is quite similar, despite the large range in peak luminosity, indicating that it is the radius of the emitting photosphere, and therefore the expansion velocity that is the main driver of the luminosity diversity. The contribution of NIR *JHK* bands to the quasi-bolometric flux for SN 2020kyg is ~ 4 per cent at -3 d, rising steadily to ~ 30 per cent at $+30$ d. The *u*-band contribution on the other hand drops from ~ 40 per cent at -3 d to ~ 15 per cent at $+30$ d. The time-dependent fractional contribution of the optical (*griz*), UV (*u*), and NIR (*JHK*) bands to the bolometric flux is shown in Fig. 5.

In order to derive explosion parameters such as the ^{56}Ni mass (M_{Ni}), total ejecta mass (M_{ej}), and kinetic energy (E_k), we fit the bolometric light curves of SN 2020kyg and other SNe Iax with an Arnett model (Arnett 1982), using the analytical treatment formulated by Valenti et al. (2008). The opacity was fixed at $\kappa_{\text{opt}} = 0.07 \text{ cm}^2 \text{ g}^{-1}$. For a homogeneous ejecta density with a photospheric velocity of v_{ph} , the kinetic energy of the explosion (Arnett 1982) can be expressed as

$$E_k \approx \frac{3}{5} \frac{M_{\text{ej}} v_{\text{ph}}^2}{2}.$$

We use the constraints from spectroscopic observations to fix v_{ph} . For SN 2020kyg, v_{ph} was fixed at 4500 km s^{-1} , the Si II $\lambda 6355$

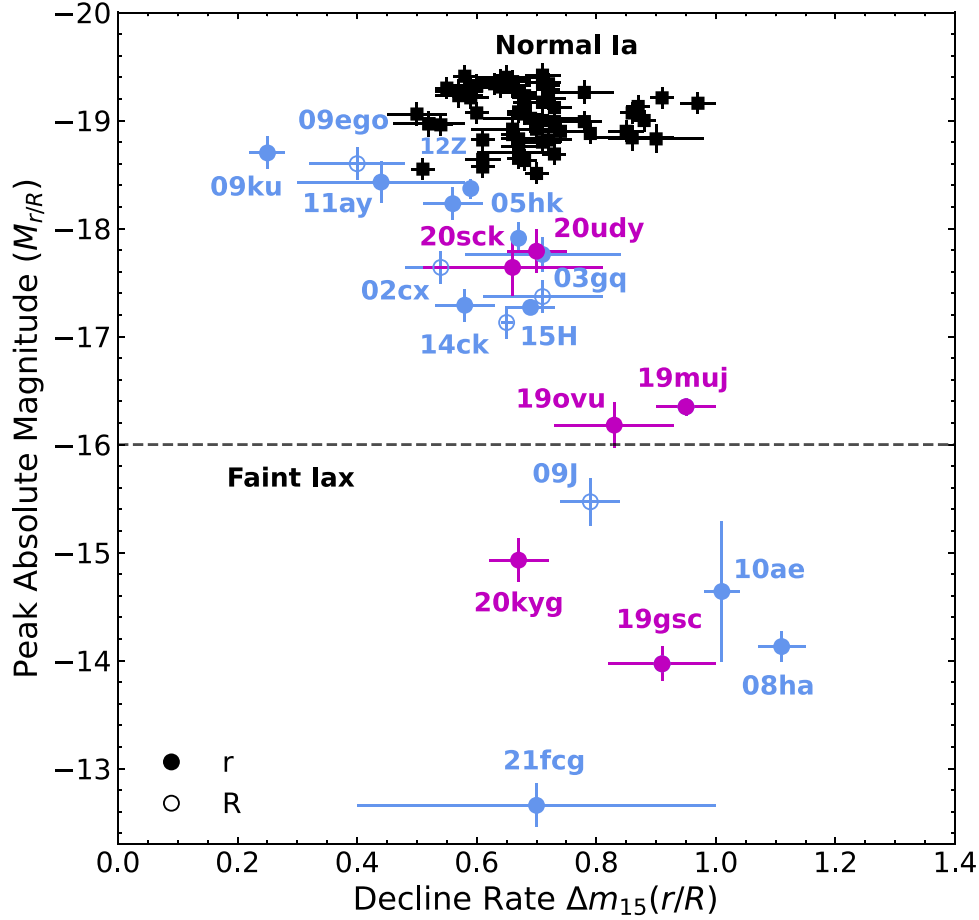


Figure 4. Peak absolute magnitude (r or R -band) versus the decline rate parameter Δm_{15} for well-studied SNe Iax (blue or magenta). Also shown (black) is the population of normal SNe Ia from the low redshift CSP sample (Stritzinger et al. 2011; Krisciunas et al. 2017). The SNe Iax highlighted in magenta are those from our ATLAS 100 Mpc Local Volume Survey (see Section 5).

velocity measured from the $-3.1d$ spectrum. The free parameters in the fitting procedure are therefore M_{Ni} , M_{ej} , and the rise time t_{R} . Fitting the $ugrizyJHK$ quasi-bolometric light curve of SN 2020kyg with this model yields best-fitting parameters of $M_{\text{Ni}} = 0.007 \pm 0.001 M_{\odot}$, $M_{\text{ej}} = 0.36^{+0.08}_{-0.06} M_{\odot}$, and $t_{\text{R}} = 9.8 \pm 1.5$ d. This g -band rise time implies that the epoch of explosion was MJD 58988.0 ± 1.5 , consistent with the pre-discovery constraints from ATLAS and ZTF (Section 3.1). The kinetic energy of the explosion is then $E_{\text{k}} = 4.4^{+2.2}_{-1.5} \times 10^{49}$ erg. The uncertainties were estimated by computing the best-fitting parameters for a range of v_{ph} values between 4000 and 5000 km s^{-1} . The M_{Ni} is a factor of ~ 100 lower than that for normal SNe Ia. However, the inferred M_{ej} is only a factor of a few lower than M_{Ch} . This extreme ratio of $M_{\text{Ni}}/M_{\text{ej}}$ is a feature of faint SNe Iax that makes it challenging for a theoretical interpretation involving a thermonuclear explosion. The disparity is illustrated in the narrow light curve of the Kromer et al. (2015) model compared to the data in Fig. 5.

4 SPECTRAL EVOLUTION

The spectral evolution of SN 2020kyg between -3 and $+54$ d relative to g -band maximum is shown in Fig. 6. A summary of spectroscopic observations is presented in Table 3. Apart from the lower velocities, spectra of SNe Iax around maximum are generally similar to normal

SNe Ia and bluer 1991T-like SNe, showing rather weak Si II and prominent Fe III (Foley et al. 2013; Jha 2017). SN Iax spectra start diverging from normal SN Ia spectra at later epochs, showing a combination of forbidden emission lines and permitted P-Cygni lines persisting for over a year after explosion (Jha et al. 2006; Foley et al. 2014). The low observed velocities in SNe Iax, especially in faint Iax, lead to spectra with narrow, resolved lines that are otherwise blended in normal SNe Ia (Foley et al. 2013), resulting in complex spectra rich in features.

The early spectra of SN 2020kyg are characterized by a blue continuum and narrow P-Cygni features of intermediate mass elements (IMEs) and iron group elements (IGEs). The spectra are compared to the faint Iax SNe 2008ha (Valenti et al. 2009), 2010ae (Stritzinger et al. 2014), and 2019gsc (Srivastav et al. 2020), the intermediate luminosity Iax SN 2019muj (Barna et al. 2021) and the luminous Iax SN 2005hk (Chornock et al. 2006; Phillips et al. 2007) in Fig. 7. The spectra at these epochs are overall quite similar, although in SN 2005hk the Si II features are shallower and the C II $\lambda 6580$ feature is less prominent. The C II $\lambda 7234$ feature is also clearly detected in the $-3.1d$ spectrum of SN 2020kyg. In the pre-maximum phase (Fig. 7, left-hand panel), C II is particularly conspicuous (except for SN 2005hk), being comparable in strength to Si II $\lambda 6355$. Additionally, the ‘W’ feature around 5500 \AA , attributed to blended features of Si II $\lambda 5454, 5640 \text{ \AA}$ (Hachinger, Mazzali & Benetti 2006), tends to be stronger in fainter SNe Iax. Srivastav et al. (2020) could not

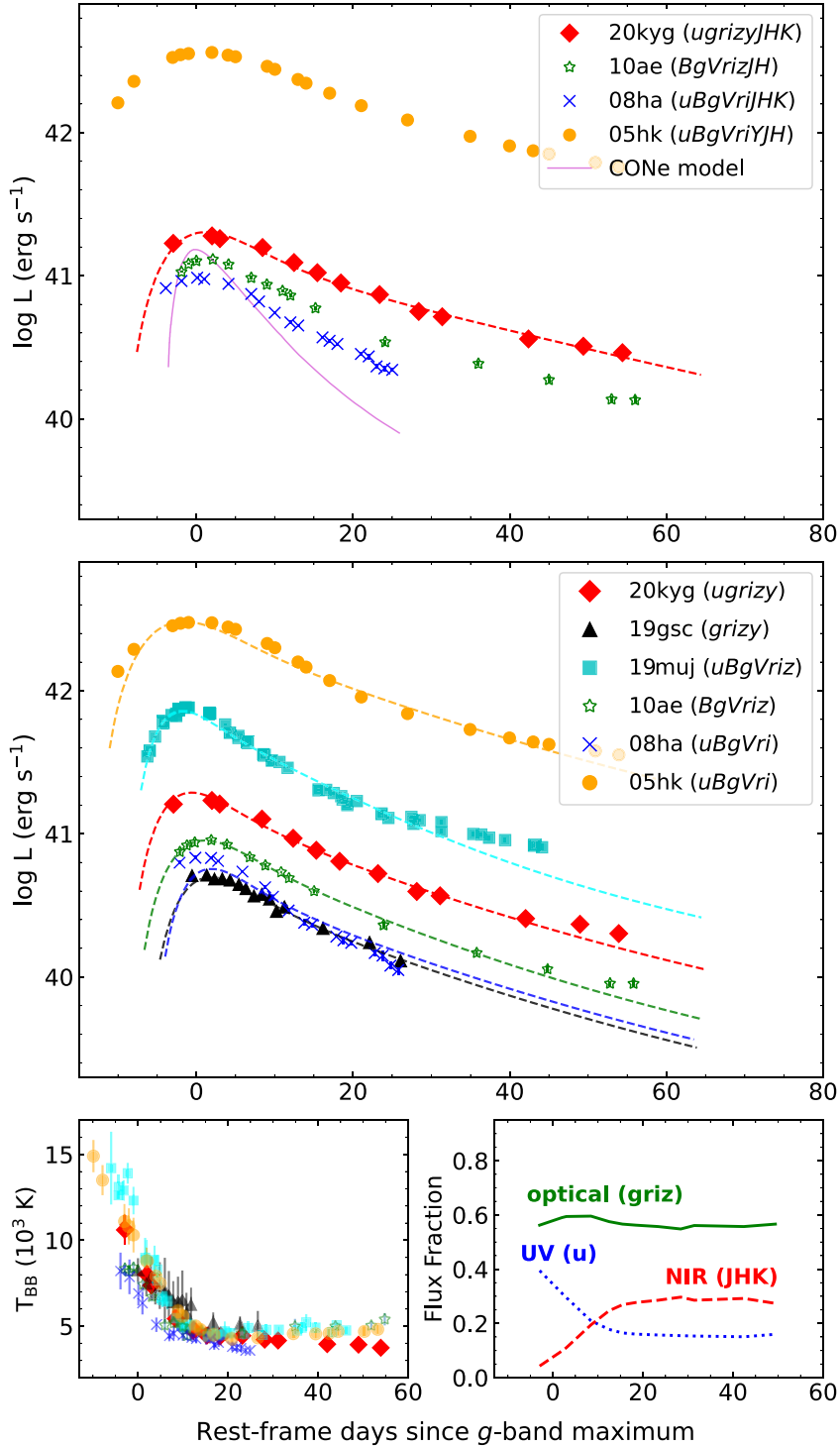


Figure 5. Top panel: quasi-bolometric light curve of SN 2020kyg integrated within the full observed *ugrizyJHK* wavelength interval. The dashed line indicates the best-fitting Arnett model used to derive the explosion parameters. Shown for comparison are the quasi-bolometric light curves of Iax SNe 2010ae, 2008ha, and 2005hk, all having NIR photometric coverage. The solid magenta line is the angle-averaged synthetic bolometric light curve for the hybrid CONe WD deflagration model (Kromer et al. 2015). Middle Panel: UV-optical quasi-bolometric light curve of SN 2020kyg integrated within *ugrizy* bands, along with quasi-bolometric light curves of Iax SNe 2019gsc (Srivastav et al. 2020), 2019muj (Barna et al. 2021), 2010ae (Stritzinger et al. 2014), 2008ha (Foley et al. 2009; Stritzinger et al. 2014), and 2005hk (Phillips et al. 2007), integrated within similar wavelength intervals for a direct comparison. Also shown are the best-fitting Arnett models for each SN. Bottom left panel: evolution of the derived blackbody temperature for SN 2020kyg and the comparison sample from fitting the SED. Bottom right panel: evolution of fractional contribution of the UV (u), optical ($griz$), and NIR (JHK) bands to the bolometric flux for SN 2020kyg.

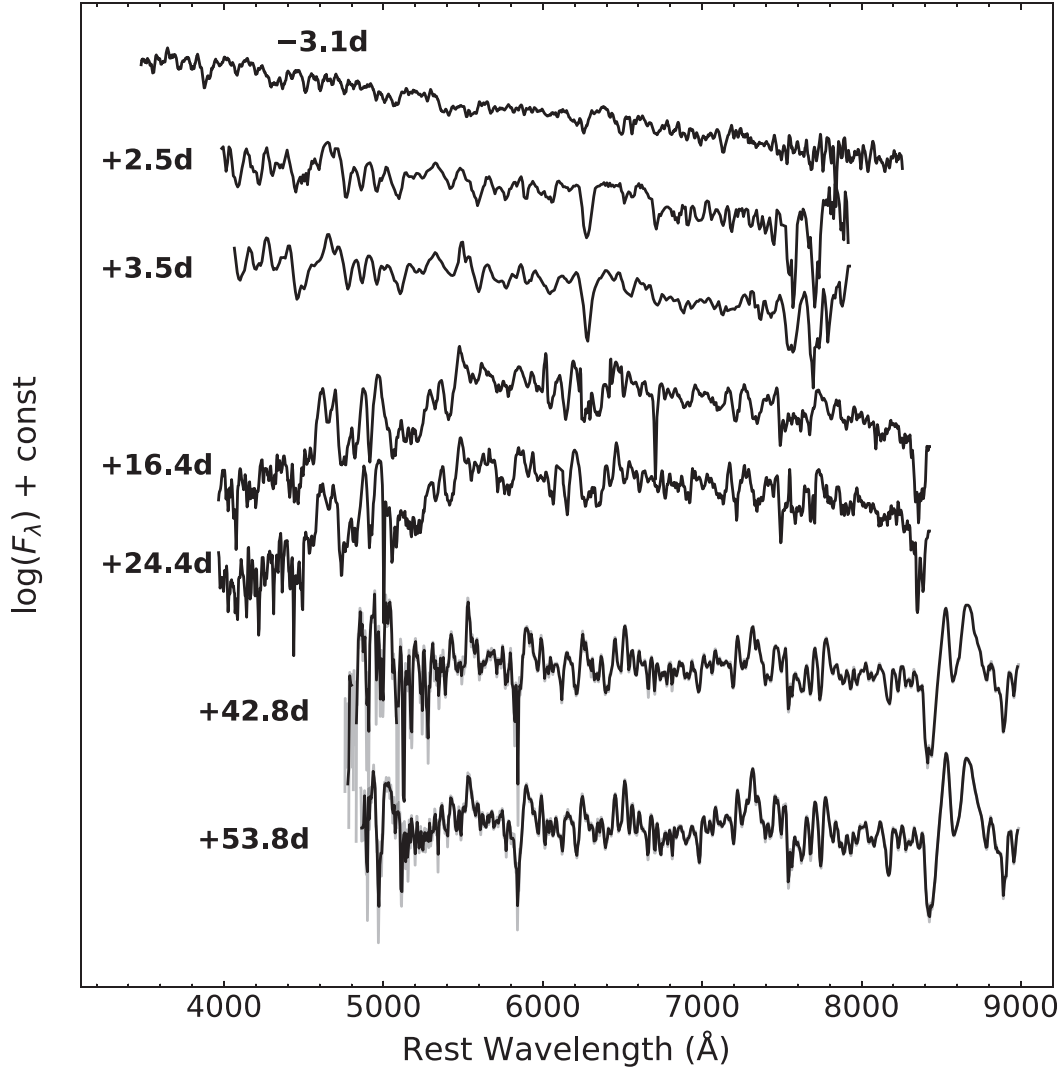


Figure 6. Spectral evolution of SN 2020kyg between -3 and $+54$ d relative to the epoch of g -band maximum.

Table 3. Log of spectroscopic observations for SN 2019gsc. The phase is relative to the epoch of g -band maximum in the SN rest frame.

Date (yyyy-mm-dd)	MJD	Phase (d)	Instrument	Exposure (s)
2020-05-25	58994.4	-3.1	FTN/FLOYDS-N	3600
2020-05-30	59000.0	$+2.5$	LT/SPRAT	2100
2020-05-31	59001.0	$+3.5$	LT/SPRAT	2100
2020-06-13	59013.9	$+16.4$	NOT/ALFOSC	3×900
2020-06-21	59021.9	$+24.4$	NOT/ALFOSC	3×900
2020-07-10	59040.3	$+42.8$	Gemini/GMOS-N	4×350
2020-07-21	59051.3	$+53.8$	Gemini/GMOS-N	4×580

adequately reproduce this feature in their TARDIS models for SN 2019gsc with a reasonable sulphur abundance of 25–50 per cent of the silicon mass fraction (e.g. Kromer et al. 2015). It is possible that other species such as Cr II and Sc II are contributing to this feature in the lower luminosity Iax events.

The -3.1 d spectrum also shows an absorption trough at ~ 4500 Å that we tentatively identify as a blend of Si III 4553, 4568, and 4575 Å lines. This doubly ionized Si feature, indicative of a hot photosphere, has been identified in pre-maximum spectra of

SN 1991T (Saselli et al. 2014). Si III features have also been identified previously in SNe Iax, such as in the optical spectra of SN 2005hk (Sahu et al. 2008) and the NIR spectra of SN 2014ck (Tomasella et al. 2016). The C II features, although very prominent in the -3.1 d spectrum, are weak or absent in the $+2.5$ and $+3.5$ d spectra of SN 2020kyg (Fig. 7, right-hand panel). The features around 6500 Å in the $+2.5$ and $+3.5$ d spectra thus likely have contribution from Co II (Jack, Baron & Hauschildt 2015; Szalai et al. 2015; Tomasella et al. 2016). In general, SNe Iax tend

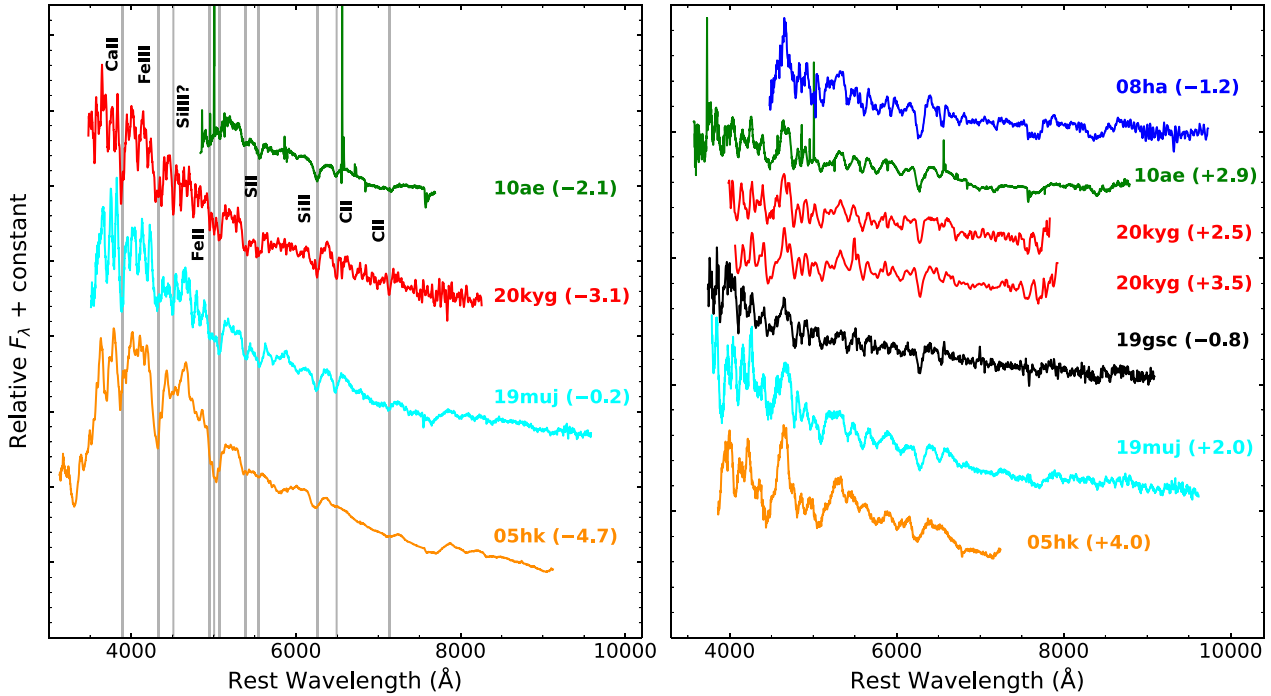


Figure 7. Spectral comparison of SN 2020kyg with spectra of faint Iax events SNe 2008ha (Valenti et al. 2009), 2010ae (Stritzinger et al. 2014) and 2019gsc (Srivastav et al. 2020), the intermediate luminosity Iax SN 2019muj (Barna et al. 2021) and the luminous Iax SN 2005hk (Chornock et al. 2006; Phillips et al. 2007). Phases are in days relative to *g*-band maximum for SNe 2020kyg and 2019gsc, and relative to *B*-band maximum for the rest.

to display stronger C II features in pre-maximum spectra relative to normal SNe Ia at similar phases as shown by Foley et al. (2013), who found signatures of C II in > 82 per cent of their Iax sample.

Figs 8 and 9 show the spectra of SN 2020kyg between +16 to +54 d, along with spectra of the comparison sample. At these later epochs, the spectra are increasingly dominated by permitted and forbidden features of Fe II, Co II, and Ca II. The Si II λ 6355 feature is weak in the +16.4 and +24.4 d spectra. The Ca II NIR triplet is prominent in the +42.8 and +53.8 d spectra, similar to SN 2008ha. These later epochs also show the emergence of forbidden [Ca II] λ λ 7292, 7324 emission, although this feature is not as pronounced as in the case of SN 2008ha, where this feature is already quite strong in the +36 d spectrum. The +54 d spectrum of SN 2019gsc obtained by Tomasella et al. (2020) showed a strong forbidden Ca II λ λ 7292, 7324 doublet, very similar to SN 2008ha. This highlights a more rapid evolution in SNe 2008ha and 2019gsc.

4.1 Expansion velocity

The Si II λ 6355 velocity evolution of SN 2020kyg and other Iax in our comparison sample is shown in Fig. 10. The Si II λ 6355 velocity of SN 2020kyg evolves from \sim 4400 km s $^{-1}$ at -3.1 d to \sim 3600 km s $^{-1}$ at +3.5 d. The C II λ 6580 velocity at -3.1 d is \sim 4000 km s $^{-1}$, lower than the Si velocity. The expansion velocities were deduced using a Gaussian fit routine implemented using `specutils`. The ratio between the C II λ 6580 and Si II λ 6355 velocities at pre-maximum epochs maximum is known to be slightly above unity in normal SNe Ia (Parrent et al. 2011; Folatelli et al. 2012), with both features showing a parallel evolution and the C II velocity typically staying

\sim 1000 km s $^{-1}$ higher. This is consistent with a spherically symmetric explosion where unburnt carbon would be expected in the outer layers of the ejecta. This velocity ratio is \sim 0.9 for SN 2020kyg, and has been observed to be lower than unity for most SNe Iax that have pre-maximum spectra with reliable C II identifications (e.g. Tomasella et al. 2020). Interestingly, this ratio is much lower (0.5–0.6) in the low luminosity Iax events SNe 2008ha and 2019gsc (Tomasella et al. 2020). Parrent et al. (2011) interpreted this as an effect of asymmetry in the ejecta, with carbon distributed in clumps not along the line of sight.

Although a correlation between peak luminosity and ejecta velocity, with more luminous SNe Iax showing higher ejecta velocities has been suggested (McClelland et al. 2010; Foley et al. 2013), notable outliers like SN 2009ku (Narayan et al. 2011) and SN 2014ck (Tomasella et al. 2016) would argue against a single parameter description of this family.

4.2 Spectral modelling

We use the fast 1D Monte Carlo radiative transfer code TARDIS (Kerzendorf & Sim 2014; Kerzendorf et al. 2019) to model the early photospheric spectra of SN 2020kyg. TARDIS assumes a sharp inner boundary or photosphere emitting a blackbody continuum. The expanding SN ejecta above this inner boundary is divided into spherical shells with user-defined density and abundance profiles. The synthetic spectrum is computed based on the interaction of virtual photon packets with the SN ejecta. TARDIS has been effectively used in the literature to model Iax spectra and constrain the ejecta composition and velocities (e.g. Magee et al. 2016, 2017; Barna et al. 2017, 2018, 2021; Srivastav et al. 2020). The aim of the empirical modelling is to arrive at a self-consistent model for the SN ejecta that

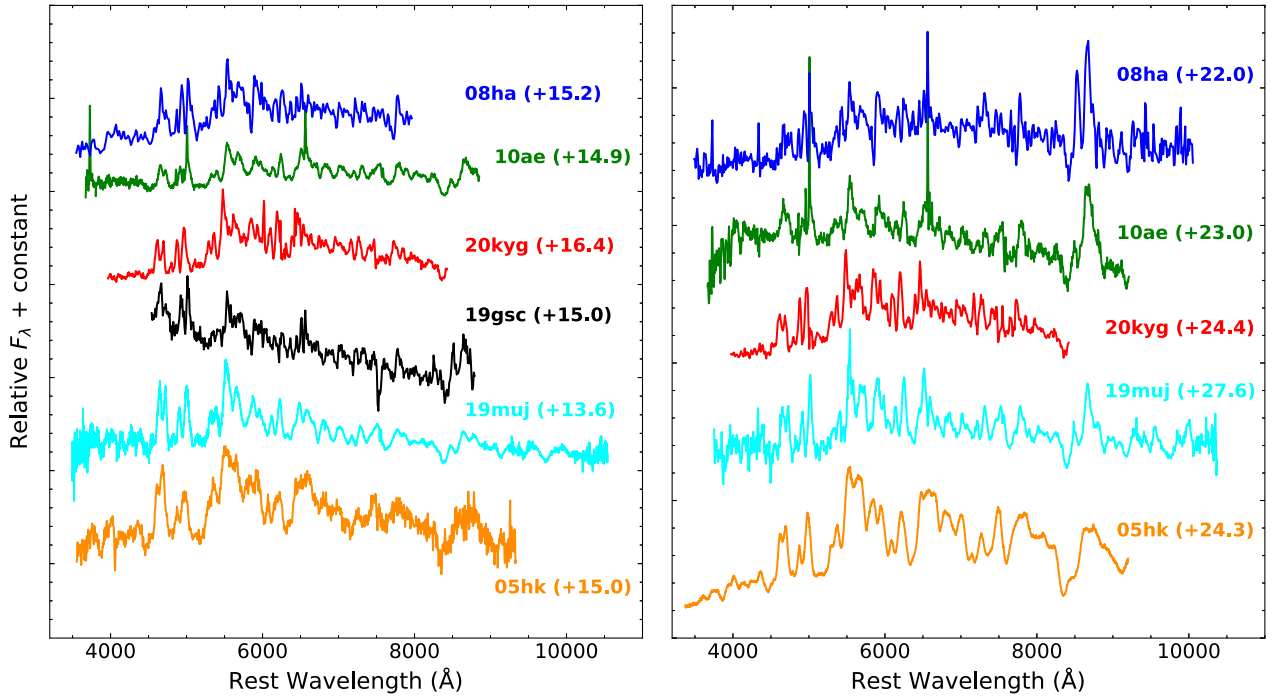


Figure 8. Spectral comparison of SN 2020kyg with SNe 2008ha (Foley et al. 2009; Valenti et al. 2009), 2010ae (Stritzinger et al. 2014), 2019gsc (Srivastav et al. 2020), 2019muj (Barna et al. 2021), and 2005hk (Phillips et al. 2007). Phases are in days relative to *g*-band maximum for SNe 2020kyg and 2019gsc, and relative to *B*-band maximum for the others.

reproduces the primary features of the photospheric spectra. Given the degeneracy between several parameters in the TARDIS model, such as central density, density profile, inner and outer velocity boundaries, mass fractions of various species etc., our model is not necessarily unique. The only parameters that were varied for an individual epoch were the time-dependent parameters, i.e. the time since explosion, inner velocity boundary of the computation volume, input luminosity (derived from the observed bolometric light curve), and mass fractions of radioactive isotopes. The outer velocity boundary was fixed at 8000 km s^{-1} . The time since explosion for each spectrum was estimated assuming the explosion epoch as MJD 58988.0, derived from the best-fitting rise time from modelling the bolometric light curve (Section 3.2). For the ejecta, we use the simplest case of a uniform abundance distribution. For SN 2019muj, Barna et al. (2021) noted that a stratified abundance did not significantly improve the fits over a uniform abundance. An exponential profile was adopted for the density, similar to SN 2019gsc (Srivastav et al. 2020), with central density $\rho_0 = 6 \times 10^{-12} \text{ g cm}^{-3}$, $t_0 = 2 \text{ d}$, and $v_0 = 3000 \text{ km s}^{-1}$, where the density is a function of time since explosion (t) and velocity (v):

$$\rho(v, t) = \rho_0 \left(\frac{t_0}{t} \right)^3 \exp(-v/v_0)$$

Our model is primarily composed of carbon, oxygen, and neon, with contribution from silicon, sulphur, magnesium, calcium, chromium, and IGEs (Table 4). We use neon as a ‘filler’ element to reduce the oxygen content, since the O I $\lambda 7774$ feature is not prominent in the observed spectra at these epochs, and adding ~ 20 per cent of neon does not produce any additional unwanted features in the synthetic spectra. The observed and synthetic spectra for -3.1 , $+2.5$, and $+3.5 \text{ d}$ are shown in Fig. 11. The Si II $\lambda 6355$ feature is relatively weak in the -3.1 d spectrum, adequately reproduced by 1 per cent

silicon in the TARDIS model, whereas the $+2.5$ and $+3.5 \text{ d}$ spectra require 3 per cent silicon. Therefore, we use a silicon abundance of 2 per cent to fit three spectra together. The ‘W’ feature at $\sim 5500 \text{ \AA}$ attributed to Si II is clearly underrepresented in the -3.1 d synthetic spectrum. The predicted sulphur yield in deflagration simulations is typically a fraction of the silicon abundance. For example, the Kromer et al. (2015) deflagration simulation predicts a sulphur to silicon ratio of 0.44. The sulphur abundance in our model is 1 per cent, whereas the silicon abundance is 2 per cent. Increasing the sulphur abundance to 10 per cent improves the fit to the red wing of the ‘W’ feature, although the blue wing is still under-fit (Fig. 11, inset). However, such a high sulphur to silicon abundance would be difficult to reconcile with theoretical predictions. SN 2020kyg shows no obvious signs of helium in the spectra. We therefore do not include helium in our model, although Magee et al. (2019) tentatively identified helium in the NIR spectrum of the faint Iax SN 2010ae.

The next observed spectrum after $+3.5 \text{ d}$ is at $+16.4 \text{ d}$ ($\sim 26 \text{ d}$ past explosion). The $+16.4 \text{ d}$ observed spectrum is already dominated by features of IGEs (Fig. 8), and the continuum shape suggests the ejecta is transitioning to an optically thin phase. The same TARDIS model computed at this epoch produces a poor fit to the continuum and features of the data. Pure deflagrations are expected to produce thoroughly mixed ejecta, suggesting that radioactive material is likely to be present in the outer layers (Kromer et al. 2013). TARDIS assumes the material within the computation volume to be in radiative equilibrium, i.e. there are no radioactive energy sources above the inner velocity boundary. This assumption becomes progressively poor as the photosphere recedes within the ^{56}Ni rich layers of the ejecta (Kerzendorf & Sim 2014), especially in the pure deflagration scenario, where ^{56}Ni is already expected to be present in the outer layers. This might explain why our model produces a poor match to the $+16.4 \text{ d}$ spectrum.

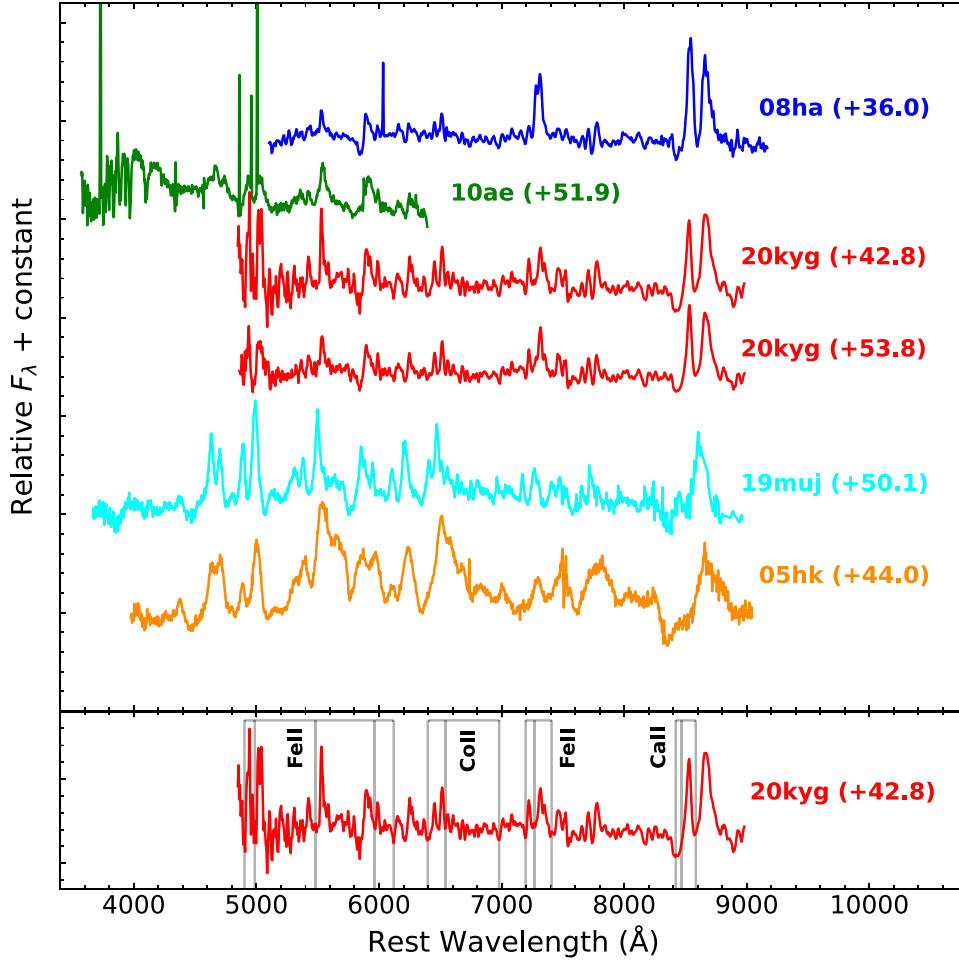


Figure 9. +42.8 and +53.8d spectra of SN 2020kyg with spectra of SNe 2008ha (Valenti et al. 2009), 2010ae (Stritzinger et al. 2014), 2019muj (Barna et al. 2021), and 2005hk (Phillips et al. 2007) at similar epochs for comparison. Phases are in days relative to g -band maximum for SNe 2020kyg and 2019gsc, and relative to B -band maximum for the others.

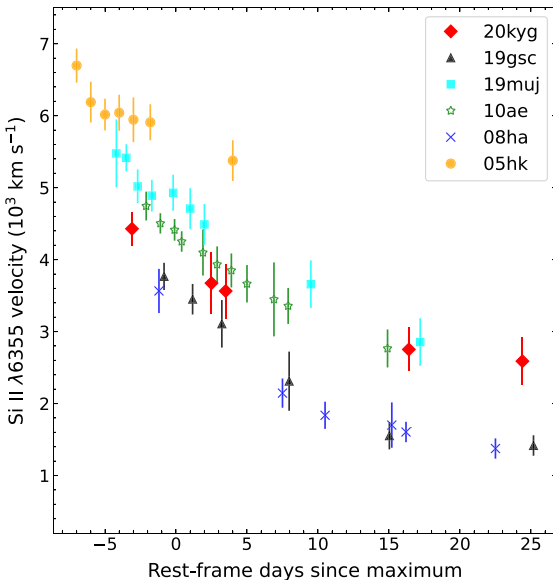


Figure 10. Evolution of the measured Si II $\lambda 6355$ velocity for SN 2020kyg, compared with that of SNe 2019gsc, 2019muj, 2010ae, 2008ha, and 2005hk.

We compare our +16.4 d spectrum to synthetic spectra generated using detailed radiative transfer calculations, following 3D deflagration simulations of M_{Ch} CO WDs explored by Lach et al. (2021). The synthetic spectra were computed using the ARTIS code (Sim 2007; Kromer & Sim 2009). The `r120_d5_0_Z` model (Lach et al. 2021) was chosen for the comparison. With $M_r \approx -15.6$, the model is more luminous than SN 2020kyg at peak, but it evolves faster and the luminosity is comparable to SN 2020kyg at +16 d. Unlike the TARDIS modelling, this is a forward model and no tuning or scaling was applied to the synthetic spectrum for comparing with SN 2020kyg (Fig. 12). Although the agreement is poor, the overall continuum shape is reproduced better than the TARDIS fit at this epoch. This is expected since ARTIS performs an approximate non-local thermodynamic equilibrium treatment of the plasma.

4.3 Host metallicity

We measured the emission line fluxes for a nearby H II region visible in the GMOS spectra, which is offset by ~ 0.7 kpc from the location of SN 2020kyg. The spectrum has been corrected for the Milky Way extinction. The H β line is located in the noisy blue region and we are thus unable to reliably measure the Balmer decrement from the

Table 4. Mass fractions of different chemical elements and other parameters used to generate the synthetic TARDIS spectra models for SN 2020kyg. v_{inner} denotes the inner boundary of the computation volume and t is the time since explosion. The emergent luminosity (L) was fixed by interpolating the bolometric light curve at the relevant epochs.

t (d)	L ($\log L/L_{\odot}$)	v_{inner} (km s^{-1})	X(C)	X(Ne)	X(O)	X(Si)	X(S)	X(Fe)	X(Co)	X(Ni)	X(Ca)
6.5	7.80	4200	0.60	0.20	0.17	0.02	0.01	10^{-3}	10^{-4}	10^{-4}	4×10^{-5}
12.1	7.83	3400	0.60	0.18	0.17	0.02	0.01	10^{-3}	10^{-4}	0.02	4×10^{-5}
13.1	7.82	3300	0.60	0.18	0.17	0.02	0.01	10^{-3}	10^{-4}	0.02	4×10^{-5}

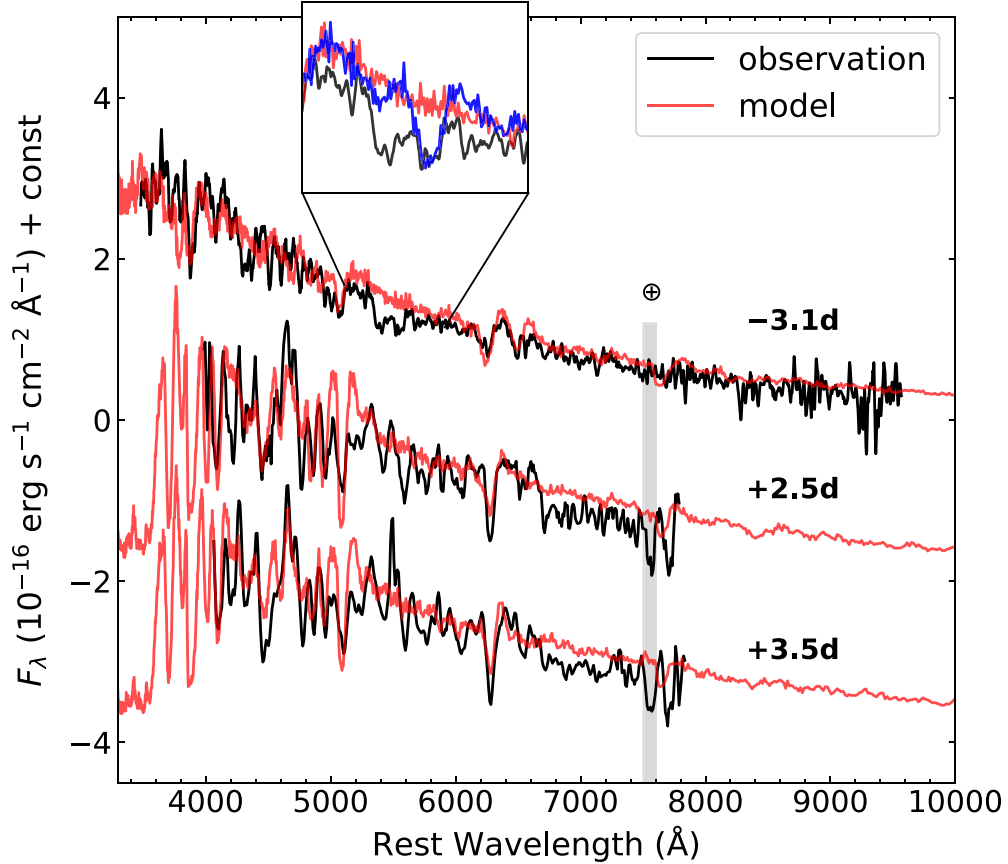


Figure 11. Early photospheric spectra of SN 2020kyg at -3.1 , $+2.5$, and $+3.5$ d (black), shown with the TARDIS models in red. The y-axis represents F_{λ} in units of $10^{-16} \text{ erg s}^{-1} \text{ cm}^{-2} \text{ \AA}^{-1}$ for the -3.1 d observed and synthetic spectra, and an offset was applied to the $+2.5$ and $+3.5$ d spectra for clarity. Inset shows how increasing sulphur abundance to 10 per cent (blue line) improves the fit to the ‘W’ feature.

ratio of $H\alpha/H\beta$. In order to estimate the metallicity, we adopted the Pettini & Pagel (2004) calibration of the N2 method, which uses the $\log([\text{N II}] \lambda 6583/H\alpha)$ ratio. It has the advantage of using two strong emission lines close to each other and thus it is not affected by host extinction. We obtain $12 + \log(\text{O}/\text{H}) = 8.68 \pm 0.04$ in N2 scale. In addition, we adopted the metallicity diagnostic of Dopita et al. (2016), which uses $[\text{N II}] \lambda 6583$, $H\alpha$, $[\text{S II}] \lambda \lambda 6717, 6731$ lines, giving $12 + \log(\text{O}/\text{H}) = 8.85 \pm 0.10$. Assuming a solar oxygen abundance of $12 + \log(\text{O}/\text{H})_{\odot} = 8.69$ (Asplund et al. 2009), we find the metallicity at this nearby H II region to be $\approx 1.0\text{--}1.5 Z_{\odot}$. This is comparable to the metallicity estimate for the Iax SN 2015H (Magee et al. 2017), and higher than the median explosion site metallicity for SNe Iax, ~ 8.5 dex (Lyman et al. 2018). While SNe Iax do not show a preference for sub-solar or super-solar metallicity environments in general (Magee et al. 2017), there is evidence for metal-poor environments for the faint Iax SNe 2008ha, 2010ae, and

2019gsc (Srivastav et al. 2020). Although SN 2020kyg does not seem to follow this trend, the number of events are small and it is not clear if there is a correlation between peak luminosity and metallicity.

5 VOLUMETRIC RATES OF SNE IAX

In this section, we constrain the volumetric rate of SNe Iax in the local Universe and compare it to the general Ia rate within 100 Mpc. We specifically investigate the ‘faint’ Iax subclass, where we define faint Iax events as those with peak absolute magnitude $M_r \gtrsim -16$, intermediate luminosity Iax events with $-17.5 \lesssim M_r \lesssim -16$ and bright Iax events with $M_r \lesssim -17.5$. There have been suggestions that these faint Iax SNe represent a physically distinct class of explosions and the volumetric rate

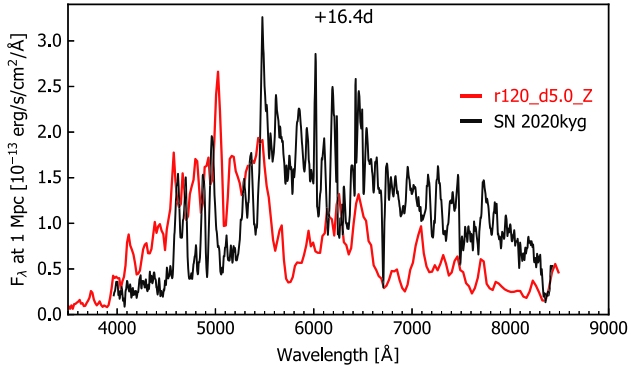


Figure 12. +16.4 d spectrum of SN 2020kyg compared to a synthetic spectrum computed using ARTIS, corresponding to the `r120_d5.0_Z` model of Lach et al. (2021).

is an important diagnostic tool for probing potential progenitor scenarios.

5.1 ATLAS local volume survey

We have constructed a 3.5 yr sample of transients within a distance of 100 Mpc detected by the ATLAS survey (including transients discovered by other surveys), during 2017 September 21 (MJD 58017) and 2021 March 21 (MJD 59294). We will present a series of papers describing the full methodology and data sets, and we briefly describe the ‘ATLAS Local Volume Survey’ here. There will be many objects in common with the ZTF Bright Transient Survey (Perley et al. 2020), but our method of selecting objects with no magnitude constraint and association with host galaxies is different. De et al. (2020) present the first results from a volume-limited approach with ZTF. We take the classifications as listed on the IAU TNS which tend to be mostly from the ZTF broad effort and PESSTO (Smartt et al. 2015, and its subsequent ePESSTO and ePESSTO + incarnations). Comparison of results from ATLAS and ZTF, with different data, selection criteria, and definitions will provide interesting discussion.

On a typical night with two operating ATLAS units, we find 10–15 real transient candidates (excluding variable stars, AGN, known movers, etc.) in the data stream. As described in Smith et al. (2020b), after processing and filtering, these are registered on the TNS as ‘good’ objects by a human scanner. A subset of these good objects are found to be associated with galaxies having a known redshift $z \lesssim 0.025$, corresponding to $D \lesssim 100$ Mpc. The radius of association with galaxies of known redshift is set at 50 kpc. When transients are found at large radial offsets, they are often background SNe, which are easily removed with a close inspection of Pan-STARRS or SDSS images combined with spectra and the ATLAS light curves of the transients. The sample also includes confirmed SNe where the host galaxy redshift was unknown, but the SN redshift reported on the TNS, usually inferred from template matching tools such as SuperNova IDentification (SNID; Blondin & Tonry 2007), GELATO (Harutyunyan et al. 2008), DASH (Muthukrishna, Parkinson & Tucker 2019), or Superfit (Howell et al. 2005) was within our cut-off. In some cases the spectrum of the transient contained narrow emission lines from the host, providing a secure redshift. We adopt $H_0 = 70 \text{ km s}^{-1} \text{ Mpc}^{-1}$ and apply a strict cut off $z \leq 0.024$ (corresponding to a comoving distance of 102 Mpc). The adopted redshift z for each transient is the associated host galaxy redshift if available, else the object redshift from the classification spectrum, as reported on

the TNS. The sample contains a total of 902 transients, of which 134 were without any spectroscopic data on TNS. The full volume-limited sample will be described in detail in a forthcoming paper (Srivastav et al., in preparation).

The sample contains only six transients spectroscopically classified as SNe Iax. Of these, two are faint Iax – SNe 2019gsc (Srivastav et al. 2020) and 2020kyg. The four additional events that were classified as Iax in the sample are SNe 2019ovu (Ihanec et al. 2019), 2019muj (Hiramatsu et al. 2019), 2020sck (Prentice et al. 2020), and 2020udy (Nordin et al. 2020). Polynomial fits to the ATLAS light curves suggest peak absolute magnitudes of $M_o = -16.35 \pm 0.10$ for SN 2019ovu, $M_o = -17.66 \pm 0.16$ for SN 2020sck, and $M_o = -17.81 \pm 0.15$ for SN 2020udy (corrected only for Galactic extinction). SN 2019muj is a well-observed event with peak $M_r = -16.35 \pm 0.08$ (Barna et al. 2021). SN 2020sck was studied in detail by Dutta et al. (2021), who reported $M_R = -17.93 \pm 0.22$. SNe 2020sck and 2020udy are bright Iax comparable to SN 2002cx (Fig. 4), while SNe 2019ovu and 2019muj are of intermediate luminosity but above our threshold to be considered as a part of the faint, low luminosity class of type Iax explosions. We note here that SN 2021feg (Karambelkar et al. 2021), the faintest Iax event to date, was discovered within our 3.5 yr window. However, it was not detected by ATLAS three times at 5σ significance on any single night, although ATLAS forced photometry does reveal 3σ detections during four epochs. Therefore, we do not include it in our sample statistics.

5.2 A search for further SNe Iax in the spectroscopically classified sample

Since SN Iax spectra around maximum light are similar to SN Ia spectra, with the lower velocity being the primary distinction (Foley et al. 2013), there is a possibility that a few SNe Iax were misclassified as normal SNe Ia. In order to investigate this further, we analysed the *o*-band light curves for each of the 269 SNe Ia in our sample through ATLAS forced photometry (Shingles et al. 2021). A total of 73 were either old SNe Ia discovered well after peak with declining light curves, or did not have adequate coverage in ATLAS around peak for a reliable light-curve fit. The remaining 196 light curves were fit with a low-order polynomial function to estimate the time of *o*-band peak. For all these Ia events with at least one rising point on the ATLAS light curve and a minimum of four points around peak, the phase of the classification spectrum, with respect to the epoch of ATLAS *o*-band peak was determined. Since we are interested in measuring the velocity around maximum to discriminate between SNe Ia and Iax, only 158 events where the phase of the TNS classification spectrum was within +15 d were selected for further analysis. Also, Si II features in SN Ia spectra progressively weaken after maximum and blended features due to IGEs increasingly dominate, making a reliable estimate of Si II $\lambda 6355$ velocity difficult beyond +15 d.

For the 158 SNe Ia that passed these cuts, we performed a Gaussian fit for the Si II $\lambda 6355$ feature to estimate the photospheric velocity and pseudo-equivalent width (pEW). The fitting routine performs a continuum correction using points on the wings of the absorption feature selected interactively by the user. The errors on velocity and pEW were computed from multiple realizations of the Gaussian fit by adding small, random offsets to the selected continuum points. In general, the fitting procedure worked well, but failed for 1991T-like events that have shallow Si features, and a few old SNe Ia that managed to sneak through, despite our rising light-curve criterion, since at later epochs this region of the spectrum is mostly dominated

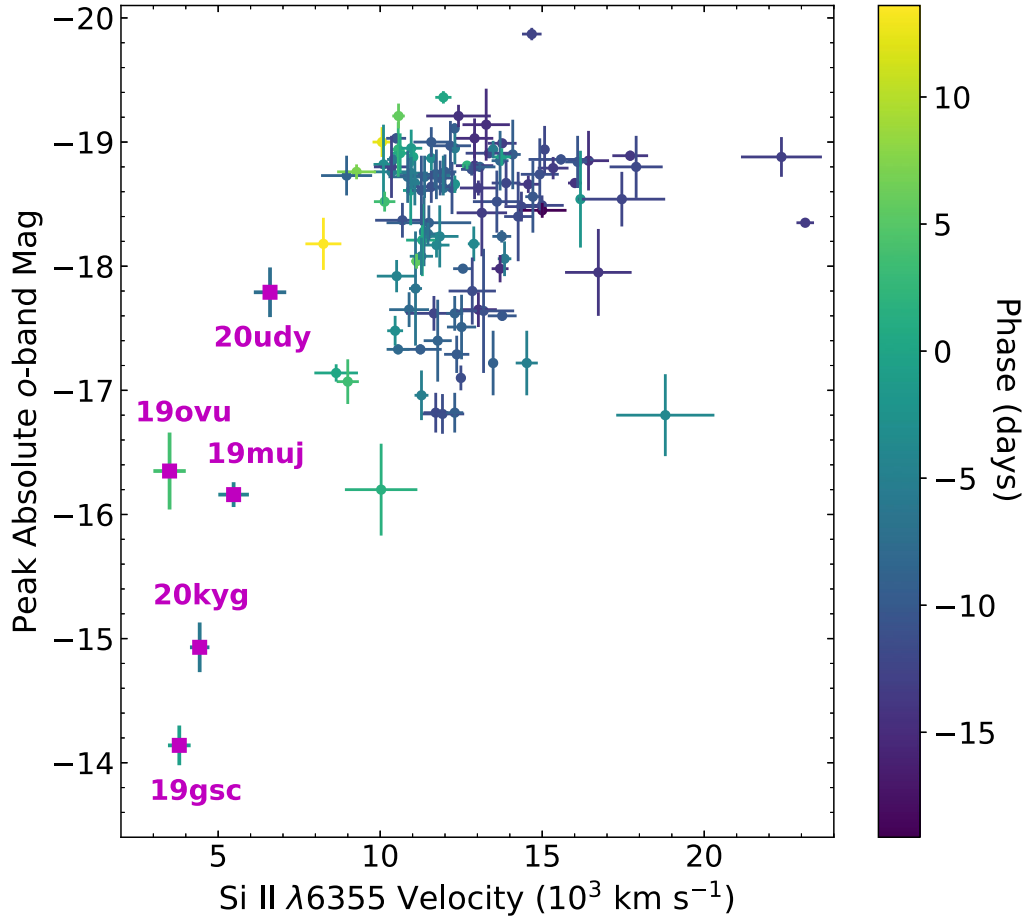


Figure 13. Peak absolute *o*-band magnitude versus the Si II $\lambda 6355$ velocity for 113 events in our sample classified as SNe Ia on the TNS. The colour map represents the phase of the classification spectrum with respect to the epoch of ATLAS *o*-band maximum. Also shown (magenta squares) are the SNe Iax in our sample, occupying a distinct region at low velocities. The colour of the error bars for the Iax in our sample represents the *o*-band phase of the spectrum that is used to deduce the Si II $\lambda 6355$ line velocity.

by blended features of IGEs. A reliable Si II $\lambda 6355$ velocity could be estimated for a total of 113 SNe Ia in our sample.

Fig. 13 shows the peak absolute ATLAS *o*-band magnitude versus the Si II $\lambda 6355$ velocity for 113 SNe Ia with classification spectra within +15 d. The phase of the classification spectrum relative to ATLAS *o*-band maximum is represented by the colour bar. None of the SNe Ia in our sample show Si II $\lambda 6355$ velocity $< 8000 \text{ km s}^{-1}$, the approximate boundary between the photospheric velocities of SNe Ia and Iax. Therefore, we do not find evidence for SNe Iax that were erroneously classified as SNe Ia in our sample. Also shown in Fig. 13 in magenta are the SNe Iax in our sample, except for SN 2020sck, as a reliable Si II velocity could not be determined from the classification spectrum. This confirms, in a volume-limited sample, that SNe Iax populate a distinct low-velocity region and are easily distinguished from the bulk of the SN Ia population.

5.3 A search for further faint SNe Iax in the unclassified sample

In general, spectroscopic classification programs are likely to select brighter objects for classification, suggesting that the likelihood of intrinsically faint transients going unclassified is higher. Also, the short rise time (~ 10 d) of faint SNe Iax means they are

usually detected around maximum, limiting the window to obtain a good-quality classification spectrum. There is a clear bias against spectroscopically classifying faint objects, and since this is a volume-limited sample, intrinsically faint objects will preferentially lack classification.

We have examined the light curves, distances, and host galaxies of all the unclassified transients in our sample to constrain how many are possibly faint Iax SNe in the ATLAS Local Volume Survey. There are 134 unclassified transients in the sample, as described in Section 5.1. The extinction-corrected peak absolute magnitude of each unclassified event was determined using the relation:

$$M_{o,c}^{\text{peak}} = m_{o,c}^{\text{peak}} - A_{o,c} - \mu$$

Here, m^{peak} refers to the peak magnitude in the ATLAS orange or cyan band, A is the Galactic extinction along the line of sight in the relevant band; $A_o \approx (A_r + A_i)/2$ and $A_c \approx (A_g + A_r)/2$, and μ is the distance modulus for the host galaxy. μ was calculated directly from the median redshift-independent distance for the host galaxy, if available on NED. In case a redshift-independent distance was unavailable, μ was estimated from the redshift (assuming $H_0 = 70 \text{ km s}^{-1} \text{ Mpc}^{-1}$). Applying a cut of $M^{\text{peak}} \geq -16$ for faint Iax candidates brings down the number to 23 unclassified events. A majority (17) of these candidates show declining light curves (i.e.

Table 5. ATLAS peak observed and absolute magnitudes of viable faint Iax candidates in the volume-limited sample that lacked a spectroscopic classification. The two confirmed faint Iax events – SNe 2019gsc and 2020kyg – are included for comparison. AT 2018aes is now a confirmed ILRT (Cai et al. 2021).

TNS name	Assumed host galaxy	Host redshift	Distance Mpc	μ Mag	Peak ATLAS Mag <i>o</i> -band	Peak Abs. Mag [†] <i>o</i> -band	Comments
AT 2018aes	NGC 5300	0.003906	20.3*	31.54	18.64 ± 0.17	−12.95	Confirmed ILRT
AT 2019dgr	NGC 2987	0.012482	54.3*	33.67	18.94 ± 0.17	−14.65	Broad LC, background SN
AT 2018kae	ESO 467- G 027	0.017401	49.9*	33.49	18.36 ± 0.17	−15.17	Slow rise, rapid decline
AT 2019bds	2dFGRS N034Z177	0.018400	75.8	34.4	18.62 ± 0.17	−15.90	Broad LC, faint Ibc?
AT 2018atw	ESO 501-IG 092	0.008613	37.2	32.85	18.35 ± 0.12	−14.62	Candidate faint Iax
AT 2020jds	NGC 7535	0.015716	49.7*	33.48	18.54 ± 0.11	−15.07	Candidate faint Iax
SN 2019gsc	SBS 1436 + 529A	0.011288	52.5	33.60	19.47 ± 0.13	−14.15	Confirmed faint Iax
SN 2020kyg	NGC 5012	0.008736	43.4*	33.17	18.23 ± 0.05	−14.97	Confirmed faint Iax

*Redshift-independent distance on NED, otherwise distance based on redshift and $H_0 = 70 \text{ km s}^{-1} \text{ Mpc}^{-1}$.

† Corrected for Galactic extinction.

peak ATLAS mag \equiv first ATLAS detection) and no recent history of non-detections prior to the first ATLAS detection, implying these are likely old SNe emerging from behind the Sun, and are thereby not considered as viable faint Iax candidates.

The six remaining candidates are listed in Table 5. AT 2018aes, has a very low luminosity of $M_o^{\text{peak}} \approx -13.0 \pm 0.2$, and a red colour, $(c - o) \sim 0.3$, and has now been conclusively quantified as an Intermediate Luminosity Red Transient (ILRT) by Cai et al. (2021). We used ATLAS forced photometry on the difference images at the positions of each of the five remaining candidates and determined the *o*-band peak magnitude and epoch using a polynomial fit (reported in Table 5). We discuss each of these below, and consider the two transients AT 2018atw and AT 2020jds as genuine faint Iax candidates.

5.3.1 AT 2019dgr

AT 2019dgr has a slowly evolving light curve, quite unlike faint Iax. It has a significant galactocentric offset of $R_g \simeq 35 \text{ kpc}$ from its assumed host NGC 2987 ($D \simeq 76 \text{ Mpc}$). This is more likely a background SN in a very faint host (undetected in both Pan-STARRS and SDSS) and unrelated to NGC 2987. The light-curve shape suggests that it is highly unlikely to be a faint SN Iax associated with NGC 2987. Thus, we rule it out as a unclassified faint Iax candidate.

5.3.2 AT 2019bds

AT 2019bds is associated with a blue, irregular host galaxy in Pan-STARRS (PSO J148.5836 – 06.4883, $g_{\text{Kron}} = 18.3$). It has a redshift of 0.018 from the 2df Galaxy Redshift Survey (Colless et al. 2003), and is a UV source (GALEXASC J095420.09-062916.7). At a projected offset of 1.9 arcsec (0.7 kpc), the association seems secure. This implies that it is more luminous ($M_o = -15.9$) and has a significantly broader light curve than known faint SNe Iax (Fig. 14). Thus, we do not consider it to be a viable faint Iax candidate.

5.3.3 AT 2018kae

AT2018kae is securely associated with ESO467-G027, being 2.4 kpc offset from the core of this Sbc spiral galaxy. The transient has quite a peculiar asymmetric light curve, with a long rise of 20 d and a rapid decline of between 5–8 d to below $o \gtrsim 20$. Since most transients are driven by a combination of ^{56}Ni decay and diffusion time-scales (leading to fast rise and exponential decay), an asymmetric light

curve with a longer rise than decline cannot easily be reproduced with a diffusion model for faint Iax SNe. We do not know the nature of this faint transient (perhaps a luminous blue variable outburst), but it is unlikely to be a faint Iax event.

5.3.4 AT 2018atw

AT2018atw is 4 kpc offset from its likely host ESO 501-IG 092. This appears to be a merging or interacting pair of galaxies with a visible tidal tail, and the 4 kpc offset would not appear unusual. At this distance, the light curve resembles a faint Iax and this remains a viable candidate (Fig. 14). The irregular host galaxy morphology is consistent with the typical late-type star-forming hosts of faint Iax, and SNe Iax in general.

5.3.5 AT 2020jds

AT 2020jds is offset by 3.7 kpc from its secure host galaxy NGC 7535. At this distance of 50 Mpc, it has a light-curve shape and peak magnitude similar to the faint Iax sample. Although we do not have pre-discovery non-detection constraints for this transient, from the light curve it appears that it was discovered around maximum. It was detected by *Gaia* the day before the ATLAS discovery, on MJD 58973 at $G = 18.81$, and again on MJD 58988 at $G = 19.89$, further indicating that we caught it on the rise to peak. We have also recovered detections in the Pan-STARRS NEO survey in the z_{P1} (with Pan-STARRS2) and w_{P1} (Pan-STARRS1) bands, which confirm the decline rate. The light curve indicates that this is a viable unclassified faint Iax candidate. The spiral host is again consistent with Iax events, rather than the early-type host galaxies typically seen for the family of calcium-strong transients (CaSTs).

After ruling out ATs 2018aes and 2019dgr, ATLAS forced photometry light curves of the remaining four unclassified candidates are shown in Fig. 14. For AT 2020jds, we also plot the *Gaia* *G*-band and Pan-STARRS2 z -band photometry. In order to perform a direct comparison for photometry in different bands, we convert the magnitudes to a monochromatic luminosity L (in erg s^{-1}), using the relation

$$L = v_{\text{eff}} \times F_{v,0} \times d^2$$

Here, v_{eff} is the effective filter frequency, d is the assumed distance to the transient, and $F_{v,0} = F_v \times 10^{0.4A_v}$ is the extinction-corrected monochromatic flux density for a Galactic extinction A_v in the relevant band.

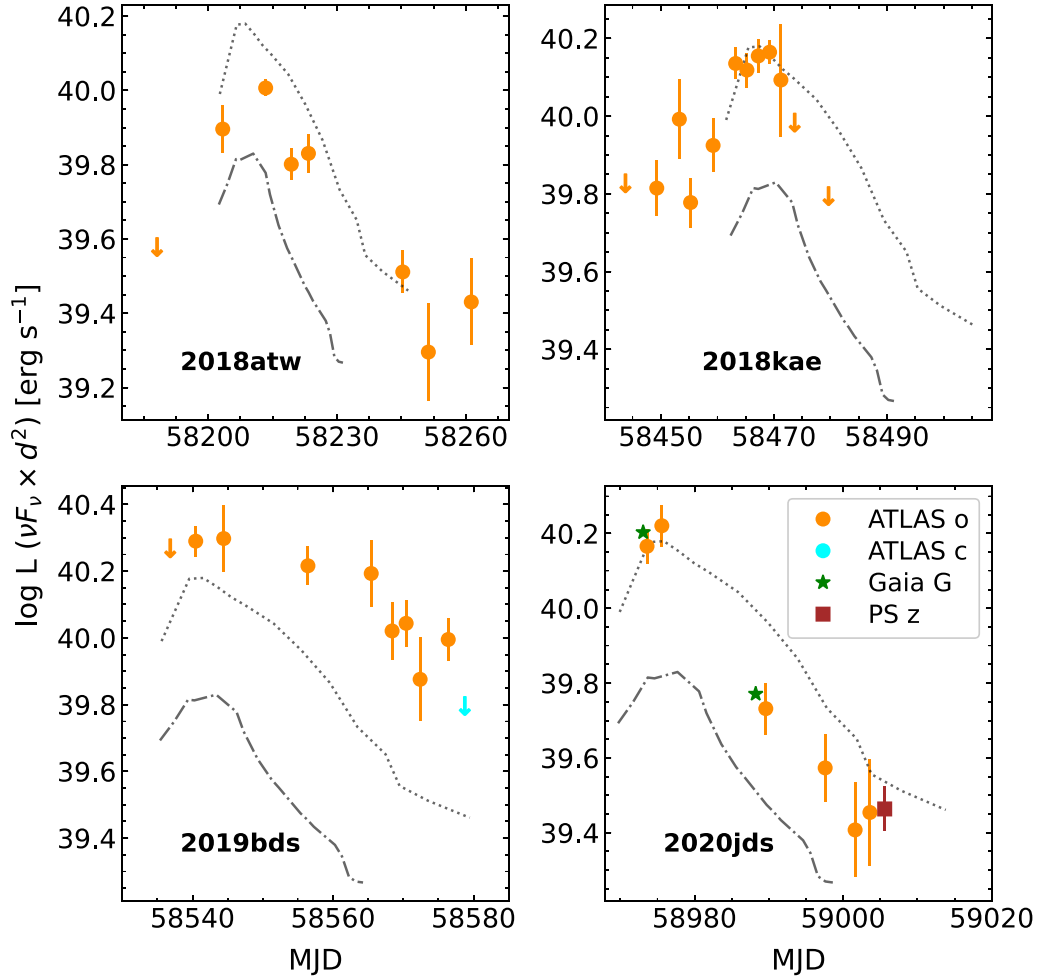


Figure 14. ATLAS forced photometry light curves of the unclassified faint transients ATs 2018atw, 2018kae, 2019bds, and 2020jds. For AT 2020jds, we also plot the available Gaia *G*-band and Pan-STARRS2 *z*-band photometry. For a direct comparison between different filters, we convert the magnitudes to a monochromatic luminosity as described in the text. Also shown are the light curves of SN 2020kyg (dotted lines) and SN 2008ha (dash-dotted lines), shifted along the time axis for comparison.

5.4 Rate calculations

The volumetric rate of a transient type is defined as:

$$R = \frac{N}{\epsilon VT} \quad (1)$$

Here, N is the number of events observed by ATLAS over time T within a volume V . The efficiency factor ϵ represents the fraction of transients of a given type that are actually detected. ϵ accounts for the intrinsic luminosity of the transient type, sky coverage, variations in sensitivity or the 5σ limiting magnitude, breaks in observation due to weather patterns, the efficiency of the machine-learning algorithm employed by the ATLAS transient server to identify real transients, and also the element of human error during the scanning process. The value of ϵ should ideally also account for any dependence of detection on the galactocentric radius of the transient. The elevated sky background noise in higher surface brightness regions will reduce sensitivity, and image subtraction artefacts in the cores of galaxies may inhibit discovery of faint transients.

We use the ATLAS efficiency simulation tool to estimate the recovery efficiency for faint Iax events (McBrien 2021). For a given input light curve, the code generates a population of simulated light curves

distributed randomly across a defined time window, redshift, and sky coordinate range, as well as performs an assessment of recovery given the history of ATLAS observations. We have quality metrics for every ATLAS image (1 427 682 exposures), including sky brightness, image quality, and most importantly the 5σ limiting magnitude. We set the ATLAS survey declination limits at $-50^\circ \leq \delta \leq 90^\circ$. No right ascension limits are set since an event in solar conjunction may still be detectable well after peak. Our efficiency simulator accounts for this, and also accounts for Milky Way extinction, since all random positions chosen have foreground Milky Way extinction associated from the Schlafly & Finkbeiner (2011) maps. The extinction in the ATLAS filters are estimated as $A_c = (A_g + A_r)/2$, and $A_o = (A_r + A_i)/2$. We do not yet account for additional internal host galaxy extinction, or the recovery efficiency as a function of galactocentric radius, although this will be implemented in future ATLAS Local Volume Survey rate papers (Srivastav et al. in preparation).

The ATLAS transient server (Smith et al. 2020b) requires a minimum of three co-spatial, 5σ detections (out of the four dithered exposures obtained over the course of an hour) on a given night to consider a detection as a real astrophysical transient. However in practice, a transient candidate that has three detections just at

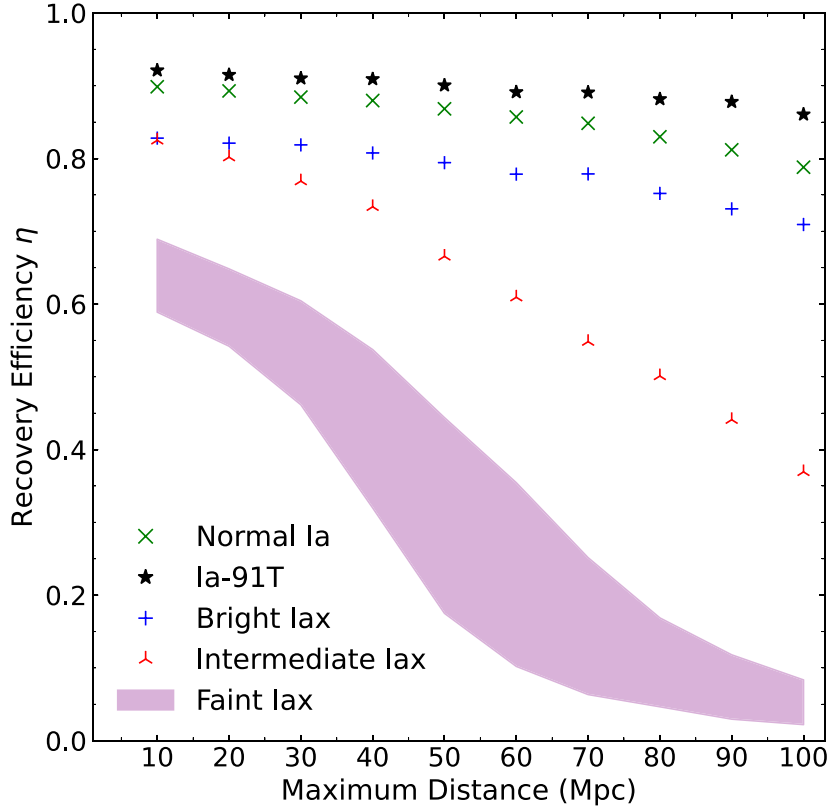


Figure 15. Simulated efficiency of recovery (η) in ATLAS for input light curves of 1991T-like Ia SN 2018cnw, normal Ia SN 2019ata, and bright, intermediate, and faint Iax light curves as a function of distance. The bright Iax used for the simulation is SN 2020udy with peak luminosity $M_o = -17.81 \pm 0.15$, whereas the intermediate luminosity Iax is SN 2019muj with peak $M_o = -16.16 \pm 0.10$. The shaded region represents the range of η for faint Iax events SNe 2020kyg and 2008ha, the latter being \sim a magnitude fainter, and faster declining compared to SN 2020kyg.

the 5σ limit on only one night is likely to be put on hold and not promoted to the TNS immediately by the human scanner. Detections on subsequent nights would tend to trigger the promotion and external registration on the TNS. To reproduce this real selection process, and effectively ensure that the simulated transient is detected on ≥ 3 different nights, we enforce a minimum of 10 detections for a simulated transient to be considered as recovered.

The fraction of recovered transients to the total number simulated gives the efficiency of recovery (η). Of the 902 events in our 100 Mpc sample, 269 are spectroscopically confirmed SNe Ia. These include 9 SN 1991T-like and 9 SN 1991bg-like Ia events. As expected, the efficiency of recovery in ATLAS is high for SN 1991T-like and normal SNe Ia light curves within 100 Mpc. The simulation suggests $\eta = 0.81$ for a normal type Ia, and $\eta = 0.86$ for a SN 1991T-like Ia, exploding at any time up to a distance of 100 Mpc (Fig. 15). However, the recovery efficiency for intermediate luminosity and faint Iax light curves is much lower, and falls off more steeply with increasing maximum distance, with $\eta = 0.35, 0.10$ for SNe 2020kyg, 2008ha, respectively, for a volume corresponding to 60 Mpc.³

Correcting for the recovery efficiency and the geometrical factor for the area of sky available to the geographical site, the SN Ia rate

within 100 Mpc from our sample (including only those classified as type Ia SNe) is:

$$R_{\text{Ia}}(\text{classified}) \approx 2.41 \pm 0.25 \times 10^{-5} \times h_{70}^3 \text{ Mpc}^{-3} \text{ yr}^{-1}$$

This is consistent with the volumetric Ia rate from PTF, $R_{\text{Ia}} = 2.43_{-0.19}^{+0.33} \pm 0.29 \times 10^{-5} \text{ Mpc}^{-3} \text{ yr}^{-1}$ (Frohmaier et al. 2019), and the ZTF Bright Transient Survey (Perley et al. 2020), who found $R_{\text{Ia}} = 2.35 \pm 0.24 \times 10^{-5} \text{ Mpc}^{-3} \text{ yr}^{-1}$. Here, $h_{70} = H_0/70$ is the correction factor for the adopted value of the Hubble’s constant. The systematic error on the SN Ia rate quoted above is derived from the error on the 100 Mpc volume V (corresponding to $z = 0.024 \pm 0.002$), and the recovery efficiency $\eta = 0.81 \pm 0.04$.

A sizeable number of transients that are almost certainly SNe lack a spectroscopic classification. Most of these have detections over multiple nights, clear association with a host galaxy within 100 Mpc, and a light curve that is consistent with being a SN. Many were unclassified as they had incomplete light curves, often in the tail phase. If we assume that the 134 unclassified candidates have the same relative fractions of different SN types as the classified sample, this would suggest an additional ~ 47 SNe Ia, implying

$$R_{\text{Ia}}(\text{total}) \approx 2.83 \pm 0.29 \times 10^{-5} \times h_{70}^3 \text{ Mpc}^{-3} \text{ yr}^{-1}$$

This is consistent with the Li et al. (2011) rate, $R_{\text{Ia}} = 3.0 \pm 0.1 \times 10^{-5} \text{ Mpc}^{-3} \text{ yr}^{-1}$, although it relies on the assumption that the unclassified sample contains similar ratios of SN types as the classified sample. For those discovered well after peak, this is likely a reasonable assumption, but further work is required, such

³The correct way of interpreting Fig. 15 is the recovery efficiency, η , within the volume enclosed by the distance (not the efficiency at that distance).

Table 6. Summary of the rate calculations for SNe Ia and SNe Iax (bright, intermediate, and faint) from the 100 Mpc ATLAS Local Volume Survey. The distance column represents the maximum distance out to which simulated transients were placed for calculating recovery efficiency. The volumetric rate computed for the spectroscopically classified events represent a lower limit. A total rate is also estimated (last column) from considering plausible candidates in the unclassified sample.

SN Type	Distance Mpc	Number of events			Recovery Efficiency	Rate ($h_{70}^3 \text{ Mpc}^{-3} \text{ yr}^{-1}$)	
		Classified	Unclassified	Total		Classified	Total
Ia	100	269	47	316	0.81 ± 0.04	$2.41 \pm 0.25 \times 10^{-5}$	$2.83 \pm 0.29 \times 10^{-5}$
Bright Iax	100	2	0.4*	2.4	0.71 ± 0.05	$2.05^{+2.70}_{-1.32} \pm 0.25 \times 10^{-7}$	$2.45^{+2.95}_{-1.39} \pm 0.27 \times 10^{-7}$
Intermediate Iax	100	2	0.8*	2.8	0.37 ± 0.08	$3.93^{+5.18}_{-2.54} \pm 1.16 \times 10^{-7}$	$5.43^{+6.19}_{-2.74} \pm 1.44 \times 10^{-7}$
Faint Iax	60	2	2	4	0.23 ± 0.13	$2.92^{+3.86}_{-1.89} \pm 1.06 \times 10^{-6}$	$5.85^{+4.62}_{-2.80} \pm 2.11 \times 10^{-6}$

*Computed by scaling the recovery efficiency with respect to that of SNe Ia, as described in Section 5.4.

as simulating the rates and confirming the number of late-phase detections expected.

Given the typical 5σ limiting magnitudes of $19 - 19.5$, ATLAS would not detect faint SNe Iax like 2019gsc and 2008ha beyond ~ 50 – 60 Mpc. We thus limit our rate calculations for faint Iax to a volume corresponding to 60 Mpc. Fig. 15 shows the efficiency of recovery that diminishes rapidly beyond 50–60 Mpc. The luminosity function for faint Iax events (shaded region in Fig. 15) is represented by SN 2020kyg (bright end) and SN 2008ha (faint end). For a distance of up to 60 Mpc, the recovery efficiencies for 2020kyg-like and 2008ha-like light curves are $\eta = 0.36, 0.10$, respectively. We thus assume a combined recovery efficiency of $\eta = 0.23 \pm 0.13$ for faint Iax. This effectively assumes a flat luminosity function with a sharp cut-off at each end. Given we have only a few well-observed events, such a simplistic function appears justified. Within 60 Mpc, the faint Iax rates, given two confirmed events are:

$$R_{\text{Iax}}(N = 2) \approx 2.92^{+3.86}_{-1.89} \pm 1.06 \times 10^{-6} \times h_{70}^3 \text{ Mpc}^{-3} \text{ yr}^{-1}$$

The asymmetric statistical uncertainties on the rate represent 1σ Gaussian errors computed from single sided upper and lower limits for small number statistics (Gehrels 1986), whereas the systematic uncertainties include the error on the recovery efficiency η . It is quite plausible, if not probable, that we are spectroscopically incomplete for faint type Iax, due a bias against spectroscopically classifying faint events. We have demonstrated that the two unclassified transients – ATs 2020jds and 2018atw – are plausible faint Iax candidates (Sections 5.3.2 and 5.3.4 and Fig. 14). Hence if these are also members of the subclass, the rate would be:

$$R_{\text{Iax}}(N = 4) \approx 5.85^{+4.62}_{-2.80} \pm 2.11 \times 10^{-6} \times h_{70}^3 \text{ Mpc}^{-3} \text{ yr}^{-1}$$

For the intermediate and bright Iax categories, it is not straightforward to estimate the number of potential unclassified candidates from their light curves, since their luminosity range overlaps with SNe Ib/c and sub-luminous SNe Ia. We compute a rough estimate for the number of unclassified candidates by scaling their recovery efficiency with respect to SNe Ia. For example, potential number of unclassified bright SNe Iax is estimated as follows:

$$N_{\text{blax}}^{\text{unclassified}} \sim \frac{N_{\text{blax}}^{\text{classified}}}{N_{\text{Ia}}^{\text{classified}}} \times N_{\text{Ia}}^{\text{unclassified}} \times \frac{\eta_{\text{Ia}}}{\eta_{\text{blax}}}$$

Here, $N_{\text{Ia}}^{\text{unclassified}} \approx 47$, as assumed above.

The volumetric rates for SNe Ia and the Iax categories are summarized in Table 6. The potential number of events from the unclassified sample estimated above is included in the systematic uncertainty for the rates of bright and intermediate SNe Iax. Since we have demonstrated robustly that there are likely to be very few intermediate and bright type Iax in the classified sample that have been missed (Fig. 13), the true volumetric rate of these types must

be low. In fact the rate of SNe Iax is dominated by the faint members of this spectroscopic class. The bright SNe Iax (see Fig. 4, $M_r \lesssim -17.5$) make up $0.9^{+1.1}_{-0.5}$ per cent of the SN Ia rate (a 2σ upper limit of ~ 3 per cent), and combined with the intermediate luminosity objects (see Table 6), the relative rate of type Iax with $M_r \lesssim -16$ is 3^{+5}_{-2} per cent.

We estimate that the faint Iax rate is much higher at 12^{+14}_{-8} per cent of the SN Ia rate and hence they dominate the volumetric rate for the inhomogeneous type Iax class. The very recent discovery of SN 2021fcg (Karambelkar et al. 2021) indicates that even fainter SNe Iax could exist, further enhancing the rates. Our simulations suggest that the recovery efficiency of a 2021fcg-like light curve is only $\eta = 0.02$ within 60 Mpc. This yields a combined $\eta = 0.19 \pm 0.17$, enhancing the faint Iax rates to 15^{+18}_{-10} per cent of the SN Ia rate. The large uncertainty is not surprising if such extremely faint objects contribute significantly to the luminosity function, since SN 2021fcg is so faint it was not independently detected in our ATLAS data. In addition, the form of the luminosity function between absolute peak magnitudes of -15 and -12 (see Fig. 4) is unconstrained.

6 DISCUSSION AND CONCLUSIONS

We have presented the results of our multiwavelength follow-up campaign for the faint Iax SN 2020kyg. We define faint SNe Iax as events with peak luminosity $M_r \gtrsim -16$. This subclass only consists of a handful of other well-observed events such as SNe 2008ha (Foley et al. 2009; Valenti et al. 2009), 2010ae (Stritzinger et al. 2014), 2019gsc (Srivastav et al. 2020; Tomasella et al. 2020), and 2021fcg (Karambelkar et al. 2021). With a peak luminosity of $-15 \lesssim M_r \lesssim -13$, these events represent the faint extremity of SN explosions.

Analytical modelling of the quasi-bolometric light curves of these events (Fig. 5) suggests ^{56}Ni masses in the range of $(1 - 7) \times 10^{-3} M_{\odot}$, roughly two orders of magnitude lower than that for normal SNe Ia. The inferred ejecta masses, in the range $0.2 - 0.4 M_{\odot}$, are not as extreme, implying very low $M_{\text{Ni}}/M_{\text{ej}}$ ratios. Fig. 16 shows M_{Ni} versus M_{ej} for different classes of thermonuclear SNe, adapted from McCully et al. (2014b, fig. 15). We also plot two points from the 3D deflagration simulations that have been calculated to try and model the full luminosity range of SNe Iax (Kromer et al. 2015; Lach et al. 2021). The models can produce M_{Ni} yields that are broadly consistent with the low inferred values for faint SNe Iax, but the predicted M_{ej} is too low when compared to the observationally inferred values. The inferred rise times are ~ 10 d for these events. For SN 2020kyg and SN 2019gsc, these inferred rise times are consistent with the constraints from pre-discovery non-detections in ATLAS and ZTF before the light curve rises.

Spectroscopically, these faint events display lower expansion velocity in general, but otherwise resemble more luminous SNe

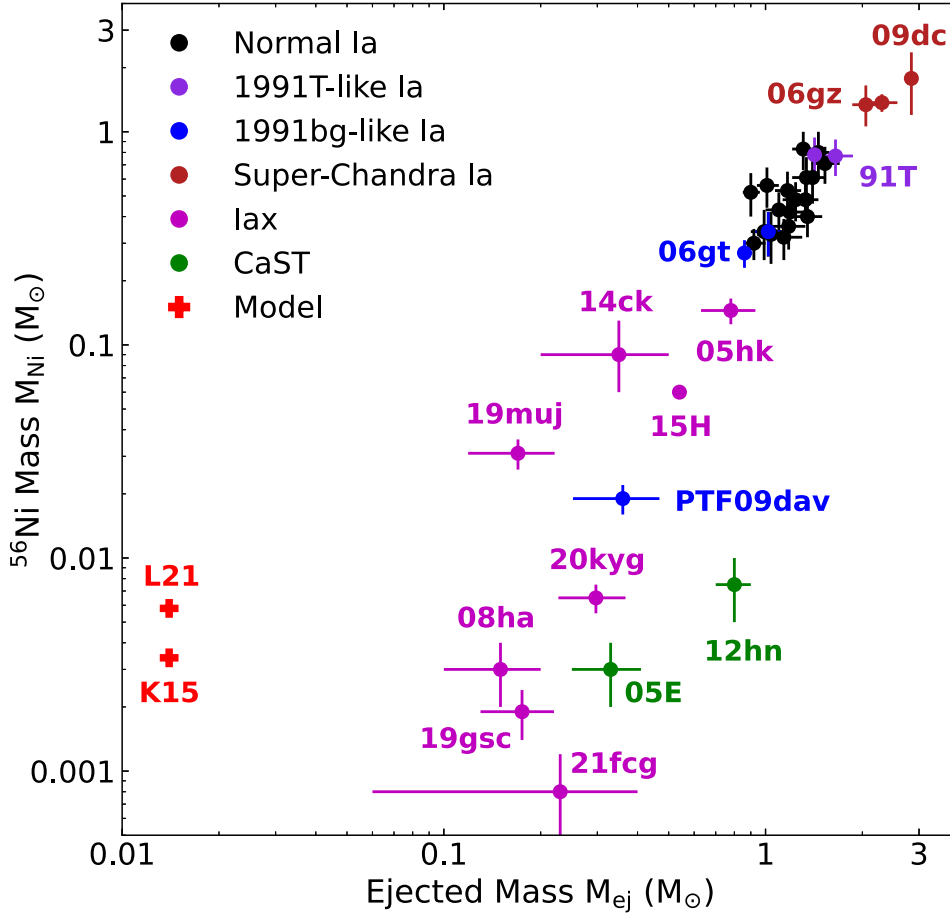


Figure 16. The $M_{\text{Ni}} - M_{\text{ej}}$ parameter space for SNe Ia and CaSTs, adapted from McCully et al. (2014b, and references therein). Additional references: normal Ia (Scalzo, Ruitter & Sim 2014), SNe 2006gt, 2006gz, 2008ec (Scalzo et al. 2019), SN 2014ck (Tomasella et al. 2016), SN 2015H (Magee et al. 2016), SN 2019gsc (Srivastav et al. 2020), SN 2019muj (Barna et al. 2021), SN 2020kyg (this work), and SN 2021fcg (Karambelkar et al. 2021). The \oplus symbols represent two of the faintest deflagration simulations in the literature – the hybrid CONe WD model of Kromer et al. (2015, or K15) and the $\tau_{114_d6.0_Z}$ model of Lach et al. (2021, or L21).

Iax albeit with more rapid evolution. We do not see evidence for interaction with circumstellar material in the spectra, and the quasi-bolometric light curves are adequately fit with a purely radioactive source of energy. The Si II $\lambda 6355$ velocity evolution (Fig. 10) displays a trend with fainter SNe Iax displaying lower velocities. Indeed, this correlation has been investigated in the literature (e.g. McClelland et al. 2010). However, more luminous members of the subclass, such as SNe 2009ku (Narayan et al. 2011) and 2014ck (Tomasella et al. 2016) displayed very low velocities $\sim 3000 \text{ km s}^{-1}$ comparable to the faint members, defying a single parameter description (Magee et al. 2017; Barna et al. 2018). We use TARDIS to model the early photospheric spectra of SN 2020kyg between -3 and $+4$ d (Fig. 11) with a simple uniform abundance model dominated by carbon, oxygen, neon, and other IMEs, similar to that used for SN 2019gsc (Srivastav et al. 2020). The same model when computed at $+16$ d produces a poor fit to the observed spectrum, which is already dominated by IGEs. This could suggest a highly mixed ejecta with significant radioactive material in the outer layers, which would limit the applicability of TARDIS at this later epoch.

The overall observed photometric and spectroscopic properties of SNe Iax, including faint Iax, suggest that these are related to SNe Ia and thus share a thermonuclear origin (Jha 2017). 3D simulations

have shown that weak deflagrations can be unsuccessful in fully unbinding the WD progenitor, leaving a compact bound remnant behind (Bravo et al. 2016). A promising pathway for faint SNe Iax is a weak deflagration involving a hybrid CONe WD (Denissenkov et al. 2013) instead of a CO WD progenitor, and 3D simulations of such a near- M_{Ch} WD by Kromer et al. (2015) show that this scenario can account for extremely low ^{56}Ni yields. This model produces a very low ejecta mass, implying the bound remnant is near- M_{Ch} . Binary population synthesis calculations have shown that hybrid CONe WDs accreting from a helium-rich donor have short delay times, as low as 30 Myr (Meng & Podsiadlowski 2014; Wang et al. 2014; Kromer et al. 2015; Liu et al. 2015). This is consistent with the results of Lyman et al. (2018), who found evidence for young stellar populations in the environments of most SNe Iax in a sizeable sample. The six Iax events in our sample are hosted by late-type, spiral, or irregular galaxies. Additionally, these hybrid CONe WDs could be more massive at formation, up to $\sim 1.3 M_{\odot}$ (Chen et al. 2014), thus requiring even shorter delay times. The blue source in pre-explosion images coincident with the location of SN Iax 2012Z was interpreted as the helium star companion of the WD progenitor (McCully et al. 2014b). This source persists in *HST* images obtained 1400 d after explosion (McCully et al. 2022). The late time flux

was found to be higher than the pre-explosion flux by a factor of two, suggesting that the bound remnant is likely contributing to this excess. We favour the hybrid CONe WD + He star scenario for explaining faint Iax events.

If the progenitors are indeed WD + He stars, the interaction of SN ejecta with the companion would be expected to strip off helium-rich material from the donor (e.g. Bauer, White & Bildsten 2019), suggesting there could be signatures of helium in late-time spectra of SNe Iax. Attempts to find helium in late-time spectra of SNe Iax have been unsuccessful so far (Jacobson-Galán et al. 2019; Magee et al. 2019). However, 3D simulations by Zeng, Liu & Han (2020) managed to strip off only $4 \times 10^{-3} M_{\odot}$ of helium from the companion, consistent with the upper limits from observations. Thus, the lack of observed helium in the spectra does not necessarily rule out its presence in the ejecta.

In order to constrain the volumetric rates of SNe Iax and in particular, faint Iax, we construct a homogeneous sample of 902 transients within a distance of 100 Mpc observed by ATLAS. The rates of SNe Iax are known to be dominated by lower luminosity events (Graur et al. 2017). Our 100 Mpc sample contains only six Iax events, of which two are faint Iax events, two intermediate luminosity and two luminous Iax events. Our derived volumetric rate for SNe Ia is $2.83 \pm 0.29 \times 10^{-5} \text{ Mpc}^{-3} \text{ yr}^{-1}$, consistent with the Lick Observatory Supernova Search rates in Li et al. (2011). The derived volumetric rate for faint SNe Iax (within 60 Mpc) is $2.92_{-1.89}^{+3.86} \pm 1.06 \times 10^{-6} \text{ Mpc}^{-3} \text{ yr}^{-1}$, accounting for 12_{-8}^{+14} per cent of the SN Ia rate. These rates are consistent with binary population synthesis calculations for CONe WD + He star systems by Wang et al. (2014), who proposed this pathway could account for 1 – 18 per cent of the Ia rate. The overall Iax rate is 15_{-9}^{+17} per cent of the SN Ia rate, clearly dominated by faint SNe Iax. Luminous Iax events like SNe 2002cx and 2005hk are relatively rare, accounting for $0.9_{-0.5}^{+1.1}$ per cent of the Ia rate.

The volumetric rates suggest there could be 40–100 SN Ia remnants in the Milky Way (Zhou et al. 2021). Given our constraints on the relative rates of SNe Iax, this would imply 3–25 Iax SNRs in our Galaxy. In the CONe WD + He star channel for SNe Iax, in addition to the partially burnt bound remnant or primary remnant (PR), the kicked companion or donor remnant, which may have evolved to the WD stage, is also expected to survive (Ruffini & Casey 2019). In principle, both PRs and DRs could be detectable in the Galaxy, although SN Ia remnants may be more difficult to detect compared to CCSN remnants (Sarbadhicary et al. 2017). Of late, a handful of WDs with peculiar velocities, unusual mass/radii, and composition with evidence of enrichment in IMEs have been discovered (e.g. Vennes et al. 2017; Raddi et al. 2018; Shen et al. 2018). These hyper velocity WDs have been interpreted as the kicked DRs from an Iax explosion. Using X-ray spectroscopy, Zhou et al. (2021) found high Mn/Fe and Ni/Fe ratios in the SNR Sgr A East, interpreting it as the surviving PR from an Iax event involving a CO WD. Thus, alongside deep pre- and post-explosion observations of nearby extragalactic SNe Iax, searching and characterizing such peculiar hyper velocity WD systems in the Galaxy is also a promising avenue for piecing together the progenitor puzzle.

ACKNOWLEDGEMENTS

SS, SJS, and SAS acknowledge funding from Science and Technology Facilities Council (STFC) grants ST/P000312/1 and ST/T000198/1. CA and JH were supported by a VILLUM FONDEN Investigator grant to JH (project number 16599). KA was supported

by Australian Research Council Centre of Excellence for All Sky Astrophysics in 3 Dimensions (ASTRO 3D), through project number CE170100013. GP is supported by ANID - Millennium Science Initiative - ICN12.009. TWC acknowledges the EU Funding under Marie Skłodowska-Curie grant H2020-MSCA-IF-2018-842471.

Pan-STARRS is a project of the Institute for Astronomy of the University of Hawaii, and is supported by the NASA SSO Near Earth Observation Program under grants 80NSSC18K0971, NNX14AM74G, NNX12AR65G, NNX13AQ47G, NNX08AR22G, and 80NSSC21K1572, as well as by the State of Hawaii.

This work has made use of data from the Asteroid Terrestrial-impact Last Alert System (ATLAS) project. The Asteroid Terrestrial-impact Last Alert System (ATLAS) project is primarily funded to search for near earth asteroids through NASA grants NN12AR55G, 80NSSC18K0284, and 80NSSC18K1575; byproducts of the NEO search include images and catalogs from the survey area. This work was partially funded by Kepler/K2 grant J1944/80NSSC19K0112 and *HST* GO-15889, and STFC grants ST/T000198/1 and ST/S006109/1. The ATLAS science products have been made possible through the contributions of the University of Hawaii Institute for Astronomy, the Queen’s University Belfast, the Space Telescope Science Institute, the South African Astronomical Observatory, and The Millennium Institute of Astrophysics (MAS), Chile.

The data presented here were obtained in part with ALFOSC under programme 61-022 (PI Angus), which is provided by the Instituto de Astrofísica de Andalucía (IAA) under a joint agreement with the University of Copenhagen and NOT.

Based in part on observations obtained with MegaPrime/MegaCam, a joint project of CFHT and CEA/DAPNIA, at the Canada-France-Hawaii Telescope (CFHT) which is operated by the National Research Council (NRC) of Canada, the Institut National des Science de l’Univers of the Centre National de la Recherche Scientifique (CNRS) of France, and the University of Hawaii. The observations at the Canada-France-Hawaii Telescope were performed with care and respect from the summit of Maunakea, which is a significant cultural and historic site.

This work was enabled in part by observations made from Gemini North telescope and UKIRT, located within the Maunakea Science Reserve and adjacent to the summit of Maunakea. We are grateful for the privilege of observing the Universe from a place that is unique in both its astronomical quality and its cultural significance. UKIRT is owned by the University of Hawaii (UH) and operated by the UH Institute for Astronomy. When the data reported here were obtained, the operations were enabled through the cooperation of the East Asian Observatory (EAO).

The Liverpool Telescope is operated on the island of La Palma by Liverpool John Moores University in the Spanish Observatorio del Roque de los Muchachos of the Instituto de Astrofísica de Canarias with financial support from the UK Science and Technology Facilities Council.

Based in part on observations obtained at the international Gemini Observatory, a program of NSF’s NOIRLab, which is managed by the Association of Universities for Research in Astronomy (AURA) under a cooperative agreement with the National Science Foundation, on behalf of the Gemini Observatory partnership: the National Science Foundation (United States), National Research Council (Canada), Agencia Nacional de Investigación y Desarrollo (Chile), Ministerio de Ciencia, Tecnología e Innovación (Argentina), Ministério da Ciência, Tecnologia, Inovações e Comunicações (Brazil), and Korea Astronomy and Space Science Institute (Republic of Korea).

This work made use of ASTROPY,⁴ a community-developed core PYTHON package for Astronomy (Astropy Collaboration 2013, 2018) and the WISEREP archive - <https://www.wiserep.org/> (Yaron & Gal-Yam 2012).

DATA AVAILABILITY

The spectroscopic data for SN 2020kyg underlying this article will be available at the WISEREP archive, <https://www.wiserep.org/>.

REFERENCES

- Arnett W. D., 1982, *ApJ*, 253, 785
- Asplund M., Grevesse N., Sauval A. J., Scott P., 2009, *ARA&A*, 47, 481
- Astropy Collaboration, 2013, *A&A*, 558, A33
- Astropy Collaboration, 2018, *AJ*, 156, 123
- Barna B., Szalai T., Kromer M., Kerzendorf W. E., Vinkó J., Silverman J. M., Marion G. H., Wheeler J. C., 2017, *MNRAS*, 471, 4865
- Barna B., Szalai T., Kerzendorf W. E., Kromer M., Sim S. A., Magee M. R., Leibundgut B., 2018, *MNRAS*, 480, 3609
- Barna B. et al., 2021, *MNRAS*, 501, 1078
- Bauer E. B., White C. J., Bildsten L., 2019, *ApJ*, 887, 68
- Bellm E. C. et al., 2019, *PASP*, 131, 018002
- Bertin E., Mellier Y., Radovich M., Missonnier G., Didelon P., Morin B., 2002, in Bohlender D. A., Durand D., Handley T. H., eds, ASP Conf. Ser., Vol. 281, *Astronomical Data Analysis Software and Systems XI*. Astron. Soc. Pac., San Francisco, p. 228
- Blondin S., Tonry J. L., 2007, *ApJ*, 666, 1024
- Bobrick A., Zenati Y., Perets H. B., Davies M. B., Church R., 2022, *MNRAS*, 510, 3758
- Bravo E., Gil-Pons P., Gutiérrez J. L., Doherty C. L., 2016, *A&A*, 589, A38
- Breeveld A. A., Landsman W., Holland S. T., Roming P., Kuin N. P. M., Page M. J., 2011, *AIP Conf. Proc.*, 1358, 373
- Brown P. J. et al., 2009, *AJ*, 137, 4517
- Brown P. J., Breeveld A. A., Holland S., Kuin P., Pritchard T., 2014, *Ap&SS*, 354, 89
- Cai Y.-Z. et al., 2021, *A&A*, 654, A157
- Chambers K. C. et al., 2016, preprint ([arXiv:1612.05560](https://arxiv.org/abs/1612.05560))
- Chen M. C., Herwig F., Denissenkov P. A., Paxton B., 2014, *MNRAS*, 440, 1274
- Chornock R., Filippenko A. V., Branch D., Foley R. J., Jha S., Li W., 2006, *PASP*, 118, 722
- Colless M. et al., 2003, preprint ([arXiv:astro-ph/0306581](https://arxiv.org/abs/astro-ph/0306581))
- De K. et al., 2020, *ApJ*, 905, 58
- Denissenkov P. A., Herwig F., Truran J. W., Paxton B., 2013, *ApJ*, 772, 37
- Dopita M. A., Kewley L. J., Sutherland R. S., Nicholls D. C., 2016, *Ap&SS*, 361, 61
- Dutta A. et al., 2021, preprint ([arXiv:2111.01226](https://arxiv.org/abs/2111.01226))
- Fernández R., Metzger B. D., 2013, *ApJ*, 763, 108
- Fink M. et al., 2014, *MNRAS*, 438, 1762
- Folatelli G. et al., 2012, *ApJ*, 745, 74
- Folatelli G. et al., 2013, *ApJ*, 773, 53
- Foley R. J. et al., 2009, *AJ*, 138, 376
- Foley R. J. et al., 2013, *ApJ*, 767, 57
- Foley R. J., McCully C., Jha S. W., Bildsten L., Fong W.-f., Narayan G., Rest A., Stritzinger M. D., 2014, *ApJ*, 792, 29
- Foley R. J., Jha S. W., Pan Y.-C., Zheng W. K., Bildsten L., Filippenko A. V., Kasen D., 2016, *MNRAS*, 461, 433
- Frohmaier C. et al., 2019, *MNRAS*, 486, 2308
- Gehrels N., 1986, *ApJ*, 303, 336
- Gehrels N. et al., 2004, *ApJ*, 611, 1005
- Gillanders J. H., Sim S. A., Smartt S. J., 2020, *MNRAS*, 497, 246
- Graur O., Bianco F. B., Modjaz M., Shivvers I., Filippenko A. V., Li W., Smith N., 2017, *ApJ*, 837, 121
- Hachinger S., Mazzali P. A., Benetti S., 2006, *MNRAS*, 370, 299
- Hakobyan A. A., Barkhudaryan L. V., Karapetyan A. G., Gevorgyan M. H., Mamon G. A., Kunth D., Adibekyan V., Turatto M., 2020, *MNRAS*, 499, 1424
- Hamuy M., Phillips M. M., Suntzeff N. B., Schommer R. A., Maza J., Aviles R., 1996, *AJ*, 112, 2391
- Harutyunyan A. H. et al., 2008, *A&A*, 488, 383
- Hiramatsu D., Arcavi I., Burke J., Howell D. A., McCully C., Pellegrino C., Valenti S., 2019, *Transient Name Server Classification Report*, 2019-1442, 1
- Hiramatsu D., Arcavi I., Burke J., Howell D. A., McCully C., Pellegrino C., Valenti S., 2020, *Transient Name Server Classification Report*, 2020-1559, 1
- Howell D. A. et al., 2005, *ApJ*, 634, 1190
- Ihanec N. et al., 2019, *Transient Name Server AstroNote*, 90, 1
- Inserra C. et al., 2018, *MNRAS*, 475, 1046
- Jack D., Baron E., Hauschildt P. H., 2015, *MNRAS*, 449, 3581
- Jacobson-Galán W. V. et al., 2019, *MNRAS*, 487, 2538
- Jha S. W., 2017, *Handbook of Supernovae*. Springer International Publishing AG, p. 375
- Jha S., Branch D., Chornock R., Foley R. J., Li W., Swift B. J., Casebeer D., Filippenko A. V., 2006, *AJ*, 132, 189
- Jordan G. C. IV, Perets H. B., Fisher R. T., van Rossum D. R., 2012, *ApJ*, 761, L23
- Karambelkar V. R. et al., 2021, *ApJ*, 921, L6
- Kashyap R., Haque T., Lorén-Aguilar P., García-Berro E., Fisher R., 2018, *ApJ*, 869, 140
- Kawabata M. et al., 2018, *PASJ*, 70, 111
- Kawabata M. et al., 2021, *PASJ*, 73, 1295
- Kerzendorf W. E., Sim S. A., 2014, *MNRAS*, 440, 387
- Kerzendorf W. et al., 2019, *tardis-sn/tardis: Tardis v3.0 alpha3*.
- Krisciunas K. et al., 2017, *AJ*, 154, 211
- Kromer M., Sim S. A., 2009, *MNRAS*, 398, 1809
- Kromer M. et al., 2013, *MNRAS*, 429, 2287
- Kromer M. et al., 2015, *MNRAS*, 450, 3045
- Lach F., Callan F. P., Bubeck D., Roepke F. K., Sim S. A., Schrauth M., Ohlmann S. T., Kromer M., 2021, preprint ([arXiv:2109.02926](https://arxiv.org/abs/2109.02926))
- Li W. et al., 2003, *PASP*, 115, 453
- Li W. et al., 2011, *MNRAS*, 412, 1441
- Liu Z.-W., Moriya T. J., Stancliffe R. J., Wang B., 2015, *A&A*, 574, A12
- Livio M., Mazzali P., 2018, *Phys. Rep.*, 736, 1
- Lyman J. D. et al., 2018, *MNRAS*, 473, 1359
- Magee M. R. et al., 2016, *A&A*, 589, A89
- Magee M. R. et al., 2017, *A&A*, 601, A62
- Magee M. R., Sim S. A., Kotak R., Maguire K., Boyle A., 2019, *A&A*, 622, A102
- Magnier E. A. et al., 2020a, *ApJS*, 251, 3
- Magnier E. A. et al., 2020b, *ApJS*, 251, 5
- Maoz D., Mannucci F., Nelemans G., 2014, *ARA&A*, 52, 107
- McBrien O. R., 2021, PhD thesis, Queen's University Belfast
- McBrien O. R. et al., 2019, *ApJ*, 885, L23
- McClelland C. M. et al., 2010, *ApJ*, 720, 704
- McCully C. et al., 2014a, *Nature*, 512, 54
- McCully C. et al., 2014b, *ApJ*, 786, 134
- McCully C. et al., 2022, *ApJ*, 925, 138
- Meng X., Podsiadlowski P., 2014, *ApJ*, 789, L45
- Muthukrishna D., Parkinson D., Tucker B. E., 2019, *ApJ*, 885, 85
- Narayan G. et al., 2011, *ApJ*, 731, L11
- Nicholl M., 2018, *Res. Notes Am. Astron. Soc.*, 2, 230
- Nordin J., Maguire K., Miller A., Perley D., Schulze S., Sollerman J., Yang Y., 2020, *Transient Name Server Classification Report*, 2020-2940, 1
- Ochner P., Pastorello A., Cappellaro E., Benetti S., Tomasella L., Elias-Rosa N., 2020, *Astron. Telegram*, 13761, 1
- Parrent J. T. et al., 2011, *ApJ*, 732, 30
- Perley D. A. et al., 2020, *ApJ*, 904, 35
- Perlmutter S. et al., 1999, *ApJ*, 517, 565
- Pettini M., Pagel B. E. J., 2004, *MNRAS*, 348, L59

⁴<http://www.astropy.org>

- Phillips M. M., 1993, *ApJ*, 413, L105
- Phillips M. M. et al., 2007, *PASP*, 119, 360
- Piascik A. S., Steele I. A., Bates S. D., Mottram C. J., Smith R. J., Barnsley R. M., Bolton B., 2014, in Ramsay S. K., McLean I. S., Takami H., eds, *SPIE Conf. Ser.*, Vol. 9147, *Ground-based and Airborne Instrumentation for Astronomy V*. SPIE, Bellingham, p. 91478H
- Poole T. S. et al., 2008, *MNRAS*, 383, 627
- Prentice S., Maguire K., Magee M. R., Deckers M., 2020, *Transient Name Server Classification Report*, 2020-2685, 1
- Raddi R., Hollands M. A., Gänsicke B. T., Townsley D. M., Hermes J. J., Gentile Fusillo N. P., Koester D., 2018, *MNRAS*, 479, L96
- Riess A. G. et al., 1998, *AJ*, 116, 1009
- Roming P. W. A. et al., 2005, *Space Sci. Rev.*, 120, 95
- Ruffini N. J., Casey A. R., 2019, *MNRAS*, 489, 420
- Sahu D. K. et al., 2008, *ApJ*, 680, 580
- Sarbadhicary S. K., Badenes C., Chomiuk L., Caprioli D., Huizenga D., 2017, *MNRAS*, 464, 2326
- Sasdelli M., Mazzali P. A., Pian E., Nomoto K., Hachinger S., Cappellaro E., Benetti S., 2014, *MNRAS*, 445, 711
- Scalzo R. A., Ruiter A. J., Sim S. A., 2014, *MNRAS*, 445, 2535
- Scalzo R. A. et al., 2019, *MNRAS*, 483, 628
- Schlafly E. F., Finkbeiner D. P., 2011, *ApJ*, 737, 103
- Shen K. J., Schwab J., 2017, *ApJ*, 834, 180
- Shen K. J. et al., 2018, *ApJ*, 865, 15
- Shingles L. et al., 2021, *Transient Name Server AstroNote*, 7, 1
- Sim S. A., 2007, *MNRAS*, 375, 154
- Singh M. et al., 2018, *MNRAS*, 474, 2551
- Skrutskie M. F. et al., 2006, *AJ*, 131, 1163
- Smartt S. J. et al., 2015, *A&A*, 579, A40
- Smith K. W. et al., 2019, *Res. Notes Am. Astron. Soc.*, 3, 26
- Smith K. W. et al., 2020a, *Transient Name Server AstroNote*, 113, 1
- Smith K. W. et al., 2020b, *PASP*, 132, 085002
- Sorce J. G., Tully R. B., Courtois H. M., Jarrett T. H., Neill J. D., Shaya E. J., 2014, *MNRAS*, 444, 527
- Srivastav S. et al., 2020, *ApJ*, 892, L24
- Steele I. A. et al., 2004, in Oschmann J. M. Jr, ed., *Proc. SPIE Conf. Ser. Vol. 5489, Ground-based Telescopes*. SPIE, Bellingham, p. 679
- Stritzinger M. D. et al., 2011, *AJ*, 142, 156
- Stritzinger M. D. et al., 2014, *A&A*, 561, A146
- Stritzinger M. D. et al., 2015, *A&A*, 573, A2
- Szalai T. et al., 2015, *MNRAS*, 453, 2103
- Takaro T. et al., 2020, *MNRAS*, 493, 986
- Taubenberger S., 2017, *Handbook of Supernovae*. Springer International Publishing AG, p. 317
- Tomasella L. et al., 2016, *MNRAS*, 459, 1018
- Tomasella L. et al., 2020, *MNRAS*, 496, 1132
- Tonry J. L. et al., 2012, *ApJ*, 750, 99
- Tonry J. L. et al., 2018, *PASP*, 130, 064505
- Tully R. B., Courtois H. M., Sorce J. G., 2016, *AJ*, 152, 50
- Valenti S. et al., 2008, *MNRAS*, 383, 1485
- Valenti S. et al., 2009, *Nature*, 459, 674
- Vennes S., Nemeth P., Kawka A., Thorstensen J. R., Khalack V., Ferrario L., Alper E. H., 2017, *Science*, 357, 680
- Wang B., Meng X., Liu D. D., Liu Z. W., Han Z., 2014, *ApJ*, 794, L28
- Waters C. Z. et al., 2020, *ApJS*, 251, 4
- Yamanaka M. et al., 2015, *ApJ*, 806, 191
- Yaron O., Gal-Yam A., 2012, *PASP*, 124, 668
- Zeng Y., Liu Z.-W., Han Z., 2020, *ApJ*, 898, 12
- Zhang M., Fuller J., Schwab J., Foley R. J., 2019, *ApJ*, 872, 29
- Zhou P., Leung S.-C., Li Z., Nomoto K., Vink J., Chen Y., 2021, *ApJ*, 908, 31

This paper has been typeset from a $\text{\TeX}/\text{\LaTeX}$ file prepared by the author.